LANDAU DAMPING OF AURORAL HISS

by

David DeWitt Morgan

An Abstract

Of a thesis submitted in partial fulfillment
of the requirements for the Doctor of
Philosophy degree in Physics
in the Graduate College of
The University of Iowa

December 1992

Thesis supervisor: Professor Donald A. Gurnett

ABSTRACT

Auroral hiss is observed to propagate over distances comparable to an Earth radius from its source in the auroral zone. In this paper the role of Landau damping is investigated for upward propagating auroral hiss. Using a ray tracing code and a simplified model of the distribution function, the effect of Landau damping is calculated as the wave propagates through the environment around the auroral zone. It is found that Landau damping puts a lower limit on the wavelength of auroral hiss. Poleward of the auroral zone, the particle energy is found in a typical case to limit the resonance energy to a value of ~ 3.2 keV or greater and to limit the wavelength to a value of about 2 km or greater. For equatorward propagation, the resonance energy must be greater than 10 keV and the wavelength must be greater than 3 km to avoid unacceptably large damping. Landau damping is found to be a likely mechanism for explaining some of the one-sided auroral hiss funnels observed by Dynamics Explorer 1, although we cannot account in detail for cases showing equatorward propagation. Upgoing electron beams of energy high enough to generate auroral hiss of the inferred

wavelengths are not usually observed. Partial transmission involving interfaces oblique

to the magnetic field is considered as a possible wavelength conversion mechanism.

Abstract approved: ⟋⟍⟍⟋ _____
Thesis supervisor

Professor, Dept. of Physics & Astronomy
Title and department

Dec 4, 1992
Date

LANDAU DAMPING OF AURORAL HISS

by

David DeWitt Morgan

A thesis submitted in partial fulfillment
of the requirements for the Doctor of
Philosophy degree in Physics
in the Graduate College of
The University of Iowa

December 1992

Thesis supervisor: Professor Donald A. Gurnett

Graduate College
The University of Iowa
Iowa City, Iowa

CERTIFICATE OF APPROVAL

———————————

PH.D. THESIS

———————————

This is to certify that the Ph.D. thesis of

David DeWitt Morgan

has been approved by the Examining Committee
for the thesis requirement for the Doctor of
Philosophy degree in Physics at the December 1992
graduation.

Thesis committee: _____
Thesis supervisor

_____
Member

_____
Member

_____
Member

_____
Member

ACKNOWLEDGEMENTS

My family also played an important role in completing this project. I thank my parents, Don and Mimi Morgan for always being available for moral support and child care and my brother Ken for his companionship. My wife Lora and my son Ben have put up with my mental and physical absence at many times, and I thank them for their forbearance.

Finally, I would thank the people of St. Andrew Presbyterian Church in Iowa City, Iowa, who have provided a reservoir of spiritual support at all times.

This work is dedicated to my family.

ABSTRACT

Auroral hiss is observed to propagate over distances comparable to an Earth radius from its source in the auroral zone. In this paper the role of Landau damping is investigated for upward propagating auroral hiss. Using a ray tracing code and a simplified model of the distribution function, the effect of Landau damping is calculated as the wave propagates through the environment around the auroral zone. It is found that Landau damping puts a lower limit on the wavelength of auroral hiss. Poleward of the auroral zone, the particle energy is found in a typical case to limit the resonance energy to a value of ~ 3.2 keV or greater and to limit the wavelength to a value of about 2 km or greater. For equatorward propagation, the resonance energy must be greater than 10 keV and the wavelength must be greater than 3 km to avoid unacceptably large damping. Landau damping is found to be a likely mechanism for explaining some of the one-sided auroral hiss funnels observed by Dynamics Explorer 1, although we cannot account in detail for cases showing equatorward propagation. Upgoing electron beams of energy high enough to generate auroral hiss of the inferred wavelengths are not usually observed. Partial transmission mechanism involving interfaces oblique to the magnetic field is considered as a possible wavelength conversion mechanism.

TABLE OF CONTENTS

LIST OF TABLES

LIST OF FIGURES

LIST OF ABBREVIATIONS

DE-1	Dynamics Explorer 1
HAPI	High Altitude Plasma Instrument
INV	Invariant latitude
keV	kilo-electron volt
kHz	kilohertz
PWI	Plasma Wave Instrument
R_e	Earth radial distance
SFC	Step Frequency Correlator
SFR	Step Frequency Receiver
UT	Universal time
VLF	Very low frequency

LIST OF VARIABLES

Γ	Integrated growth rate (nondimensional)
γ	Growth rate (Hz)
θ	Wave normal angle (angle of propagation vector with respect to magnetic field line) (radians)
θ_{Res}	Resonance cone angle (radians)
λ	Wavelength (m)
Φ_{sc}	Spacecraft potential (V)
ψ	Angle of group velocity with respect to the magnetic field line (radians)
Ω	$2\pi \times$ Cyclotron frequency (Hz)
ω	$2\pi \times$ Frequency (Hz)
ω_{pe}	$2\pi \times$ Electron plasma frequency (Hz)
A	Combination of cold plasma parameters in cold plasma determinant (nondimensional)
B	Combination of cold plasma parameters in cold plasma determinant (nondimensional)
C	Combination of cold plasma parameters in cold plasma determinant (nondimensional)
c	Vacuum light speed (m/s)
$D^{(0)}$	Cold plasma determinant (nondimensional)
E	Particle energy (eV)

F	Equilibrium distribution function normalized by plasma density (s^3/m^3)
$\mathcal{F}$	Unnormalized distribution function detected by HAPI (s^3/km^6)
f_{ce}	Electron cyclotron frequency (Hz)
f_{pe}	Electron plasma frequency (Hz)
f_{UHR}	Upper hybrid frequency (Hz)
$G_1^{\pm}$	Combinations of derivatives of the distribution function (s^4/km^7)
$G_2^{\pm}$	Combinations of derivatives of the distribution function (s^4/km^7)
k	Propagation vector (cycles/m)
L	Cold plasma parameter (nondimensional)
L_{eff}	Effective length (of antenna) (m)
m_e	Electron mass (eV/c^2)
n	Index of refraction vector (nondimensional)
$\mathcal{P}$	Spectral density of wave [$(V/m)^2/Hz$]
P	Cold plasma parameter (nondimensional)
R	Cold plasma parameter (nondimensional)
S	Cold plasma parameter (nondimensional)
s	Path length (m)
v	Particle velocity (m/s)
v_b	Beam velocity (m/s)
V_g	Group velocity (m/s)

LIST OF SUPERSCRIPTS AND SUBSCRIPTS

Superscripts

(0)	Value for cold plasma
$\pm$	+, ions; -, electrons

Subscripts

$\perp$	Perpendicular to the magnetic field line
$\parallel$	Parallel to the magnetic field line
eff	Effective
Res	Resonance cone
b	Beam
c	Cyclotron
e	Electron
p	Plasma

CHAPTER I. INTRODUCTION

Very low-frequency (VLF) hiss is defined by Helliwell (1965) as "an emission whose spectrum resembles that of band limited thermal or fluctuation noise. . . . It can be identified aurally by a hissing sound." This type of very low frequency radio noise was first noticed by radio engineers and by aurora observers during the first half of this century. Among the early observations were those of Burton and Boardman (1933), who obtained their observations from submarine transmission cables as well as a loop antenna. They were the first to note the possible coincidence of auroral flashes with a "hissing sound" picked up by their equipment. Somewhat later Ellis (1959) noted a correlation between VLF hiss and visible aurora, but as in the case of Burton and Boardman, the result was strictly qualitative. The first quantitative study of the relation of VLF hiss to the visible aurora was made by Morozumi (1962). In his Master's Thesis, Morozumi used measurements in the Antarctic taken with photometers, an all-sky camera, and radio receiving equipment to correlate VLF hiss with homogeneous arc and band type aurora around magnetic midnight.

With the advent of orbiting spacecraft as research vehicles, it became possible to study the phenomenon of auroral hiss closer to its source. Using data from the low-altitude satellite Injun 3, Gurnett (1966) performed the first orbiting spacecraft study of what is now called auroral hiss. Gurnett's paper established the standard

characteristics of auroral hiss, namely, the strong correlation with intense fluxes of field-aligned electrons of energies less than 10 keV, the location near the edge of the 40-keV electron trapping boundary, and the characteristic V shape of hiss on a frequency--time spectrogram. It was also asserted that the emissions were approximately symmetric about the base of the funnel, but it was implied in the abstract to this paper that in some cases the hiss was attenuated on one side. In a later paper, Gurnett and Frank (1972) again showed the association of auroral hiss with electrons less than 10 keV in energy and correlated the occurrence of auroral hiss with electron inverted-V events. These papers showed that auroral hiss was associated with the auroral regions, and specifically related to low-energy electron beams occurring within the auroral zones.

The V or funnel shape of auroral hiss as seen on a frequency-time spectrogram is an easily observed characteristic that immediately identifies the radio noise as auroral hiss. It is a direct result of the fact that auroral hiss propagates in the whistler mode very close to the resonance cone. A funnel-shaped spectrum from the Dynamics Explorer 1 (DE-1) spacecraft is shown in Figure 1. This event took place on September 18, 1981. The base of the funnel in this case is located at about 0752 universal time (hereinafter UT) or 69.8° invariant latitude (hereinafter INV). Poleward of the base of the funnel a sharp upper frequency cutoff is observed in the spectrum. This cutoff occurs for whistler mode radiation at the lesser of the local electron plasma or cyclotron frequency (Gurnett et al., 1983). Note that the funnel extends both

poleward and equatorward of the base of the funnel. Gurnett et al. (1986) established a clear connection between the base of the funnel and the source field line for hiss generated artificially by an electron gun aboard Spacelab 2. The funnel base is generally taken to indicate the L shell or invariant latitude of the source.

Smith (1969) first suggested that the V shape could be produced by propagation at wave normal angles near the resonance cone. This idea was convincingly demonstrated in a number of papers, starting with Mosier and Gurnett (1969). In this paper, ray tracing was performed that accurately reproduced the funnel shape of the spectrogram. Other papers with similar comparisons include James (1976), Gurnett et al. (1983), Lin et al. (1984), and Farrell et al. (1988). The previously mentioned active experiment aboard Spacelab 2 also demonstrated that such V-shaped spectrums could be generated by an artificially produced electron beam (Gurnett et al., 1986).

The generation mechanism of auroral hiss was initially thought to be incoherent Cerenkov radiation from a beam of precipitating electrons. Ellis (1957) first claimed that the power generated by such a beam could be sufficient to generate the auroral hiss observed on the ground. Later, however, Taylor (1973) showed that incoherent Cerenkov radiation falls some two orders of magnitude below the observed spectral density. Maggs (1976) attempted to explain the observed power in natural auroral hiss events with a convective beam instability. However, his explanation depends heavily on auroral arc geometry. In the case of the hiss generated by an electron gun during the Spacelab 2 mission, Farrell et al. (1988) demonstrated that the power generated by

the incoherent Cerenkov process was insufficient by seven orders of magnitude to generate the observed power. Farrell et al. (1989) then showed that sufficient power could be generated by a plasma bunching instability of the electron beam. Farrell et al. (1989) also pointed out that the mechanism proposed by Maggs fails for two reasons to explain the observed spectral density of the Spacelab 2 hiss: first, the calculated wavelength is much bigger than the source region, and, second, the wave passes through the source region too quickly to grow to large amplitudes. The most likely generation mechanism for auroral hiss appears to involve an intermediate beam-plasma instability as put forward in Farrell et al. (1989). Mosier and Gurnett (1969) used data from the low-altitude spacecraft Injun 5 to determine the Poynting flux direction of auroral hiss. The auroral hiss was shown to be propagating downward along the field line, the same direction as the electron beam. Farrell et al. (1988) again demonstrated in the Spacelab 2 active experiment that $\mathbf{k} \cdot \mathbf{v}_{beam} > 0$. From these findings, a strong case can be made that auroral hiss is generated entirely at the $m = 0$ or Landau resonance ($v_{\parallel} = \omega/k_{\parallel}$), since cyclotron resonance interactions would have propagation vectors directed opposite to the motion of the beam.

The purpose of this paper is to explore the effect of Landau damping on the propagation of auroral hiss. Landau growth or damping is a collisionless process by which electromagnetic waves exchange energy with electrically charged particles around the resonance velocity $v_{\parallel} = \omega/k_{\parallel}$. It is important to study Landau damping because (1) Landau damping is an important factor in determining the intensity of waves in the

magnetosphere, and (2) the absence of Landau damping may put constraints on the properties of the wave, particularly the wavelength. In Section II, we will look at the observed intensity characteristics of auroral hiss. Spectrograms of specific events will be presented. In Section III, the formula for the wave growth rate γ (i.e., the negative of the damping coefficient) will be simplified for the case of propagation near the resonance cone and a spherically symmetric electron distribution function. Some sample distribution functions will be discussed. In Section IV, the ray tracing procedure utilized will be discussed. In Section V, sample rays will be traced and the damping computed for each ray. Energy and frequency dependence of the damping will be tested. Finally, in Section VI the implications of the results from Section V will be discussed.

The data utilized for the present research is from the Dynamics Explorer 1 (DE 1) spacecraft. DE 1 was launched on August 3, 1981, into a circumpolar orbit with a geocentric apogee 4.65 R_E and a perigee 1.09 R_E and with an orbital period of 6 h 49 min. The apogee rotates about the Earth at a rate of 108°/year so that over a period of several years it is possible to survey all geocentric distances between apogee and perigee at all latitudes. The spacecraft rotates in a "reverse cartwheel" configuration with a period of 6 s. These orbital parameters are documented by Gurnett and Inan (1988). Because of spacecraft rotation, fields and particles can be sampled as a function of direction as well as position. The instrument used to detect plasma wave phenomena is the Plasma Wave Instrument, described by Shawhan et al. (1981). The

instrument consists of a Step Frequency Correlator (SFC), composed of two Step Frequency Receivers (SFRs), and several other receivers. The data of primary interest to us are from the SFC, which operates between 0.1 and 400 kHz. This frequency range is divided into 4 channels, each of which is divided into 32 steps. Thus, the total frequency range of the instrument is divided into 128 logarithmically spaced steps with 1% resolution. In its usual mode of operation, the SFC samples the entire spectrum once every 32 s. The SFC receiver noise level is about 10^{-16} V^2/m^2 Hz, well below the intensity of most auroral hiss events. The SFC can receive data from several input devices, the most important for our purpose being the long wire X-axis antenna, which rotates in the spin plane of the spacecraft. This antenna is 200 m long with an effective length of $L_{eff} = 101.4$ m for detecting long wavelength electric fields ($\lambda >> L_{eff}$).

The instrument on DE 1 that provided the plasma data used for this work is the High Altitude Plasma Instrument (HAPI), described by Burch et al. (1981). This instrument was designed to detect particles of energy/charge between 5 eV and 32 keV. This energy range is divided into 64 logarithmically spaced steps with energy resolution of 32%. The instrument can be programmed to sample every 2n-th step, n being selected by the observer. The usual mode of operation is one energy sweep per 0.5 s. The instrument consists of 5 electrostatic analyzers oriented at 45°, 78°, 90°, 102°, and 135° to the spin axis of the spacecraft. All detectors are used to detect ions, whereas only the 78°, 90°, and 102° detectors are used to detect electrons. Each detector has a full-width half-maximum acceptance angle of 10° in the azimuthal

direction and 2.5° in the polar angle direction. Because the Earth's magnetic field dipole is oriented about 12° from the Earth's rotation axis and because the resonance cone in the sampled region is about 6°, it is highly probable that one of the 78°, 90°, and 102° detectors is always sampling the loss cone.

Several sets of software were utilized in this project. Spectrograms and contour plots were produced using either the Southwest Data Display and Archival System (SDDAS) created by J. D. Winningham's group or similar software created by Dr. J. L. Burch's group, both at Southwest Research Institute (SwRI), in San Antonio, Texas. Distribution functions were obtained from the same sources. All programs used in the analysis of data were written by the author.

CHAPTER II. ATTENUATION CHARACTERISTICS OF
AURORAL HISS

The top panel of Figure 1 shows the classical signature of auroral hiss on a frequency-time spectrogram. The intensity is indicated by a color bar, with red being most intense, and dark blue being least intense. This particular case is chosen as an example because the "funnel" shape of the spectrum is unobscured by other types of electromagnetic noise, attenuation, or multiple sources. The base of the funnel is at about 69.8° INV, and the funnel extends more or less symmetrically from this invariant latitude in both directions. The source of the auroral hiss is assumed to be on the field line where the base of the funnel occurs, i.e., about 69.8° INV. A variable upper cutoff is visible in the auroral hiss spectrum, more clearly at higher than at lower invariant latitudes. This cutoff is due to the local plasma frequency dropping below the emission frequency of the auroral hiss, which leads to a propagation cutoff. The bottom panel shows the electron distribution during the same period. The electron distribution is depicted here on an energy-time spectrogram. The distribution function is indicated by a color bar, with red being most intense, dark blue being least intense, and black indicating intensity below the range of the color bar. The transition between the polar cap and the auroral zone is quite sharp at about 69.8° INV, the same invariant latitude as the auroral hiss source. The electron distribution function undergoes another

abrupt transition at 67.5° INV as the spacecraft enters the plasma sheet. The plasma sheet electrons, which map magnetically to the current sheet, change on a larger scale and appear to be less energetic than the auroral zone electrons, but they are still more energetic than the polar cap electrons. As the spacecraft passes out of the auroral zone and into the polar cap, the auroral hiss goes through a minimum in intensity but then recovers and continues to propagate to the south through the plasma sheet.

Figure 2 shows a set of wave and particle spectrograms similar to those in Figure 1 for an auroral hiss event on September 26, 1981. Although the electric field spectrogram does not show the symmetrical auroral hiss funnel with the clarity of the previous spectrogram, it is a more typical auroral hiss event in several ways. The source region is obscured by broadband electrostatic noise (Gurnett and Frank, 1977) so that the base of the funnel is not readily observed. Although funnel shapes are visible both to the north and the south of the auroral region, it is likely that they do not have the same base, i.e., there are multiple sources of auroral hiss in this event. The auroral hiss propagates unattenuated to the north in this event and is not cut off by the local plasma frequency, although there is some variation in the intensity in this region. Finally, although the auroral hiss funnel is visible to the south (i.e., toward lower invariant latitudes), it fades out. Note that this fading out shows no indication of the sharp cutoff feature that is so obvious northward of the source in Figure 1. Instead, the decrease in intensity is gradual, indicating an absorption of energy as the wave moves away from its source region. Over the polar cap, the electron distribution

function falls off sharply around 1 keV. The auroral zone, from about 69° INV to 67° INV exhibits the usual high intensity of high energy electrons. The auroral hiss funnel extends southward until it gradually dies out around 64° INV. Interestingly, the decline in intensity appears to coincide with a rise in energy of the electron distribution function.

Figure 3, for an auroral hiss event of October 5, 1981, shows many of the same features as the previous event. Northward, essentially unattenuated propagation coincides with an electron distribution function that falls off at low energy. Southward, the hiss appears to be attenuated abruptly as it leaves the auroral zone. This attenuation almost coincides with a bump in the distribution function around 68.5° INV. Again, the plasma sheet electrons are more energetic than the polar cap electrons although they are not as energetic as the auroral zone electrons. Also, the plasma sheet electrons change on longer time scales than the auroral zone electrons. In this spectrogram, it is fairly obvious that we are looking at multiple source locations for auroral hiss. There appears to be a more or less continuous source between 71° and 69° INV. There is apparently a discrete source around 68.6° INV and very probably a weaker source near 68.0° INV. Finally, although the auroral hiss is observed to be attenuated abruptly at about 67.5° INV, it is not totally obliterated; there is still a trace of auroral hiss that continues to propagate southward. In this case, equatorward attenuation appears to take place in an almost discrete region which may or may not coincide with a rise in electron energy.

Finally, for completeness, we show a dayside case of auroral hiss attenuation. Figure 4 shows an event at 1000 UT on September 26, 1981. As in Figure 1, the funnel-like aspect of the auroral hiss is quite clear, more so than for a typical case. The smooth upper cutoff is due to the electron cyclotron frequency rather than the electron plasma frequency, since for dayside hiss, f_{ce} is usually less than f_{pe}. There appears to be a strong source region between 70° and 71° INV. Also, there is a visible frequency minimum around 72.2° INV, which probably indicates another source. The faint line that falls irregularly between 1000 and 1020 UT at frequencies above the funnel is upper hybrid resonance noise. When the upper hybrid frequency is well above the cyclotron frequency, as in this case, it is approximately equal to the electron plasma frequency. The auroral hiss funnel very clearly has more attenuation equatorward than poleward of the auroral zone. It is interesting to note how the attenuation compares with changes in the upper hybrid frequency (f_{UHR}). A sharp attenuation takes place at about 68.2° INV almost coincident with a fairly abrupt change in f_{UHR}. Another sharp decrease in auroral hiss intensity occurs at 65.0° INV, coincident with another possible jump in f_{UHR}. Note that there are no abrupt changes in the high energy electron distributions at these points. These coincidences indicate a possible role for density related reflections in the attenuation of auroral hiss. Note however, that there is a strong north--south asymmetry in the electron distribution. It is interesting to ask what the effect of the electrons on auroral hiss intensity ought to be.

From these examples it is possible to make some generalizations. First, auroral hiss is observed to propagate for great distances in the Earth's magnetosphere. It can be estimated from spectrograms of the type shown in this section that auroral hiss can propagate about 1.5 R_e poleward from its source in the auroral zone, in most cases with little or no attenuation. However, equatorward from the auroral zone, such long distance propagation is rarely observed. The second generalization is therefore that auroral hiss is often less intense when propagating equatorward than when propagating poleward. This assertion will be made more quantitative later in this section. Finally, it is clear that electron distributions go to higher energies equatorward than poleward of the source region.

Part of the motivation for this thesis is to explore the connection between the last two of these assertions. Do the warm plasma sheet electrons have an effect on the intensity of auroral hiss? From the discussion of the various events in this section, it seems that in some cases the energetic electrons have the effect of attenuating the auroral hiss as it propagates equatorward from the auroral zone. In that case, what constraints can be put on the characteristics of the auroral hiss from what we know about its propagation and the distribution functions? The purpose of this paper is to explore answers to these questions.

A visual study of the available DE 1 wave data was done to quantify the assertion made above that the auroral hiss is generally weaker equatorward than poleward of the auroral zone source region. To conduct this study 104 spectrograms

of auroral hiss events were selected from the DE-1 PWI data set. This data set ranges from 1981 to 1987, although the amount of available data decreases sharply with advancing years. A spectrogram was eliminated from the data set if there was no possibility of seeing both sides of the funnel. A spectrogram was also eliminated if the spacecraft was not at a geocentric radial distance of at least 2.0 R_e during detection of both sides of the funnel. This last condition is to avoid confusion of orbital effects with attenuation. This is necessary because when the spacecraft gets to low altitudes, it can go under the region where the auroral hiss is propagating. This effect leads to a shortened or even disappearing funnel.

The spectrograms were examined by eye to determine whether the intensity of the poleward propagating auroral hiss was greater or less than the equatorward propagating auroral hiss. The results were tabulated in three categories: poleward intensity > equatorward intensity, poleward intensity < equatorward intensity, and poleward intensity ~ equatorward intensity. An event was tabulated in the third category if there was any doubt at all which side of the auroral hiss funnel was brighter. In the case of an "eyeball average" of this sort, a difference in intensity probably requires a factor of 10 to be clearly visible. The results are shown in Table 1. This study makes it clear that there is a strong tendency for auroral hiss to propagate poleward, with generally lower intensities in the equatorward direction. Since electron populations tend to be more energetic toward the equator as the ray

enters the plasma sheet, it is very plausible that Landau damping is responsible for at least part of the observed difference.

CHAPTER III. LANDAU DAMPING

Collisionless growth or damping is the mechanism by which an electromagnetic wave exchanges energy with particles in a collisionless plasma by accelerating or decelerating them. In the simplest case, the way in which this happens can be described by saying that the charged particles in a plasma interact most strongly with a propagating field if that field is at rest in the reference frame of the particles. Thus, if a particle is moving rapidly with respect to a sinusoidally varying wave electric field, the particle is subjected to a rapidly varying force that averages to zero to a very good approximation. However, if the particle is traveling at the phase velocity of the wave, then the particle is subjected to a nearly constant force that can accelerate the particle. The simplest case, where particles traveling in one dimension interact with linearly polarized waves is discussed at length in many books on plasma physics, e.g., Nicholson (1983). This damping mechanism, when applied to Langmuir waves, is known as Landau damping (Landau, 1946). It is also possible for charged particles gyrating in a magnetic field to interact with a wave at various multiples of the cyclotron frequency. This type of damping is called cyclotron damping.

For a general particle distribution, the calculation of the damping coefficient that characterizes these processes can be exceedingly complicated. However, with suitable

assumptions, approximations can be made that make the computation of the damping coefficient tractable.

The linear growth rate (the negative of the damping coefficient) of whistler waves propagating in a homogeneous magnetized medium was derived by Kennel (1966) using standard mathematical methods to compute a very general dispersion relation. His derivation assumes resonance energies well above the thermal energy of the distribution function. The dispersion relation involves integrals over an infinite number of singular terms. With the assumption that the imaginary part of the wave frequency, i. e., the growth rate γ, is small compared to the wave frequency ω, Kennel was able to derive an expression for the growth rate that is valid at all frequencies. His formula is given below:

$$\gamma \frac{\partial D^{(0)}}{\partial \omega} = 2\pi^2 \sum_{+,-} \frac{(\omega_p^{\pm})^2}{\omega |k_{\parallel}|} \int_0^{\infty} v_{\perp} dv_{\perp} \int_{-\infty}^{\infty} dv_{\parallel} \sum_m \delta(v_{\parallel} - \frac{\omega - m\Omega^{\pm}}{k_{\parallel}})$$

$$[G_1^{\pm}((P - n^2\sin^2\theta)[2(L - n^2)J_{m+1}^2 + 2(R - n^2)J_{m-1}^2$$

$$+ n^2 \sin^2\theta \, (J_{m+1} - J_{m-1})^2] \, v_{\perp} - n^2 \cos\theta \sin\theta$$

$$\cdot \{2v_{\parallel} \, J_m[J_{m+1}(L - n^2) + J_{m-1}(R - n^2)] + n^2 \cos\theta \sin\theta$$

$$\cdot v_{\perp} (J_{m+1} - J_{m-1})^2\}) + G_2^{\pm} \{4v_{\parallel} J_m[(L - n^2)(R - n^2)$$

$$+ n^2 \sin^2\theta(S - n^2)] - 2n^2 \, v_{\perp} \cos\theta \sin\theta[(R - n^2) \, J_{m-1}$$

$$+ (L - n^2) \, J_{m+1}]\}]$$

(1)

where

$$G_1^\pm = \frac{\partial F^\pm}{\partial v_\perp} - \frac{k_\parallel}{\omega}\left(v_\parallel \frac{\partial F^\pm}{\partial v_\perp} - v_\perp \frac{\partial F^\pm}{\partial v_\parallel}\right) \tag{1a}$$

and

$$G_2^\pm = J_m\left[\frac{\partial F^\pm}{\partial v_\parallel} + \frac{m\Omega^\pm}{\omega v_\perp}\left(v_\parallel \frac{\partial F^\pm}{\partial v_\perp} - v_\perp \frac{\partial F^\pm}{\partial v_\parallel}\right)\right] \tag{1b}$$

with $k_\perp = k \sin\theta$ and $k_\parallel = k \cos\theta$, where k is the wave number. The cold plasma parameters R, L, P, and S are defined by Stix (1962) as,

$$R = 1 - \sum_s \frac{\omega_{ps}^2}{\omega^2}\frac{\omega}{\omega+\Omega_s} \tag{1c}$$

$$L = 1 - \sum_s \frac{\omega_{ps}^2}{\omega^2}\frac{\omega}{\omega-\Omega_s} \tag{1d}$$

$$P = 1 - \sum_s \frac{\omega_{ps}^2}{\omega^2} \tag{1e}$$

$$S = 1 - \sum_s \frac{\omega_{ps}^2}{\omega^2-\Omega_s^2} \tag{1f}$$

ω_{ps} is 2π times the plasma frequency and Ω_{ps} is 2π times the cyclotron frequency of species s. $n = ck/\omega$ is the index of refraction, J_m's are Bessel functions of the first kind with argument $(k_\perp v_\perp/\Omega_{ce})$, θ is the wave normal angle, and $D^{(0)}$ is the cold plasma dispersion function determinant given by

$$D^{(0)} = An^4 - Bn^2 + C \tag{2a}$$

where

$$
\begin{aligned}
A &= S \sin^2 \theta + P \cos^2 \theta \\
B &= RL \sin^2 \theta + PS(1 + \cos^2\theta) \\
C &= PRL
\end{aligned}
\tag{2b}
$$

The dispersion relation for a cold plasma is given by

$$D^{(0)} = 0 \tag{2c}$$

Equations (1c-1f) and (2a-2c) are given by Stix (1962). The superscript (0) of the determinant indicates that this is for a cold plasma. The index m refers to multiples of the cyclotron frequency in the argument of the delta function in Equation (1). This delta function gives the resonance condition, $v_| = (\omega - m\Omega^\pm)/k_|$. When m is not 0, the interaction between waves and particles is said to take place at a cyclotron resonance and is called cyclotron growth or damping. When m = 0, it is called Landau growth or damping in analogy to the case for Langmuir waves. The resonance velocity for Landau damping is given by $v_| = \omega/k_|$. Perpendicular and parallel subscripts in Equation (1) refer to components perpendicular and parallel to the magnetic field.

It can be seen from Equation (1) that in the computation of the growth rate γ each cold plasma parameter, R, L, P, or S, is compared with n^2, except in the first term, where P is compared with $n^2 \sin^2 \theta$. Auroral hiss is known to propagate near the

resonance cone, which is a surface along which the index of refraction goes to infinity. The resonance cone angle, θ_{Res}, is given by

$$\tan^2\theta_{Res} = -\frac{P}{S}$$

(3)

Since the resonance cone angle for auroral hiss is usually on the order of 1 rad, the $\sin^2\theta$ factor of the first term is usually not so small as to be worrisome, and n^2 is seen to dominate all competing terms. Typically, R, L, P, and S are no greater than 5% of their respective competing terms in n^2. Assuming that $n^2 >> R, L, P,$ and S, and that $n^2 \sin^2\theta >> P$, it is found that every term has a factor of n^4. Since we are concerned with frequencies well above the ion plasma frequency, ion effects need not be taken into account. Taking these factors into account, we get the result that

$$\gamma\frac{\partial D^{(0)}}{\partial\omega} = \frac{2\pi^2\omega_{pe}^2 n^4}{\omega|k_\|}\sum_{m=0}^{\infty}\int_0^{\infty}v_\perp\,dv_\perp\int_{-\infty}^{\infty}dv_\|\,\delta\left[v_\| - \frac{\omega - m\Omega_{ce}}{k_\|}\right]$$

$$[G_1(v_\perp\sin^2\theta\,[2J_{m+1}^2 + 2J_{m-1}^2 - \sin^2\theta\,(J_{m+1} - J_{m-1})^2]$$

$$+ \cos\theta\sin\theta\cdot\{2v_\|\,J_m[J_{m+1} - J_{m-1}]$$

(4)

$$+ \cos\theta\sin\theta v_\perp(J_{m+1} - J_{m-1})^2\})$$

$$+ G_2\{4v_\|\,J_m[1 - \sin^2\theta]$$

$$+ 2v_\perp\cos\theta\sin\theta\,[J_{m-1} + J_{m+1}]\}]$$

Using trigonometric identities and the Bessel function recursion relation

$$J_{m-1}(x) + J_{m+1}(x) = \frac{2mJ_m(x)}{x}$$

with $x = k_\perp v_\perp / \Omega_{ce}$ reduces Equation (4) to

$$\gamma \frac{\partial D^{(0)}}{\partial \omega} = \frac{2\pi^2 \omega_{pe}^2 n^4}{\omega |k_\|} \sum_{m=0}^{-\infty} \int_0^\infty v_\perp \, dv_\perp \int_{-\infty}^\infty dv_\| \, \delta \left[v_\| - \frac{\omega - m\Omega_{ce}}{k_\|} \right]$$

$$\left[G_1 \left[v_\perp \frac{4(m\Omega_{ce})^2 \sin^2\theta \, J_m^2}{k_\perp^2 v_\perp^2} + v_\| \frac{4 \cos\theta \sin\theta \, (m\Omega_{ce}) \, J_m^2}{k_\perp v_\perp} \right] \right.$$

$$\left. + G_2 \left[v_\perp \frac{4 \cos\theta \sin\theta \, (m\Omega_{ce}) \, J_m}{k_\perp v_\perp} + v_\|(4 J_m \cos^2\theta) \right] \right] \tag{5}$$

At this point it is useful to do the integration over $v_\|$. This is accomplished by substituting the resonance condition, the argument of the delta function in Equation (5),

$$v_\| = \frac{(\omega - m\Omega_{ce})}{k_\|} \tag{6}$$

into Equations (1a), (1b), and (5). Substitution of this resonance condition and the definitions of G_1 and G_2 into Equation (5) yields, after some algebra,

$$\gamma \frac{\partial D^{(0)}}{\partial \omega} = 8\pi^2 n^4 \frac{(\omega_{pe})^2}{\omega|k_{\parallel}|} \int_0^\infty v_\perp dv_\perp \sum_{m=0}^\infty J_m^2$$

$$\left\{ \left[\frac{m\Omega_{ce}}{\omega} \frac{\partial F}{\partial v_\perp} + \frac{k_{\parallel}v_\perp}{\omega} \frac{\partial F}{\partial v_{\parallel}} \right] \left[\sin^2\theta \frac{m^2\Omega_{ce}^2}{k_\perp^2 v_\perp} + \frac{\omega - m\Omega_{ce}}{k_{\parallel}} \cos\theta \sin\theta \frac{m\Omega_{ce}}{k_\perp v_\perp} \right] \right.$$

$$\left\{ \left[\frac{\partial F}{\partial v_{\parallel}} \left[1 - \frac{m\Omega_{ce}}{\omega} \right] + \frac{m\Omega_{ce}}{\omega v_\perp} \frac{\omega - m\Omega_{ce}}{k_{\parallel}} \frac{\partial F}{\partial v_\perp} \right] \left[\frac{m\Omega_{ce}}{k_\perp} \cos\theta \sin\theta + v_{\parallel} \cos^2\theta \right] \right\}$$

which further reduces to

$$\gamma \frac{\partial D^{(0)}}{\partial \omega} = \frac{8\pi^2 n^4 \omega_{pe}^2}{k^2 |\cos\theta|} \int_0^\infty dv_\perp J_m^2 \left[\frac{\partial F}{\partial v_\perp} \frac{m\Omega_{ce}}{k} + \frac{\partial F}{\partial v_{\parallel}} \cos\theta \, v_\perp \right] \qquad (7)$$

where $v_{\parallel}$ is a constant determined by Equation (6). This is a general expression for any wave propagating close to the resonance cone. It is good for cyclotron as well as Landau damping or growth. In this expression, $F = F(v_\perp, v_{\parallel})$ and the integral is carried out over $v_\perp$ while $v_{\parallel}$ is a constant determined by Equation (6).

A further simplifying assumption is made by approximating the derivative of the zeroth order dispersion relation for propagation near the resonance cone. From Equation (2a) and (2b)

$$\frac{\partial D^{(0)}}{\partial \omega} = \left(\frac{\partial A}{\partial \omega} - \frac{4A}{\omega} \right) n^4 - \left(\frac{\partial B}{\partial \omega} - \frac{2B}{\omega} \right) n^2 + \frac{\partial C}{\partial \omega} \qquad (8)$$

For resonance cone propagation, $n^2 >> R, L, P,$ and S. Generally, the cold plasma parameters and therefore A, B, and C will be of order 1 or less. Thus, the first

term will dominate all others because of the fourth power of n. Since the definition of the resonance cone requires that $A \to 0$, only one term remains to be considered:

$$\frac{\partial D^{(0)}}{\partial \omega} \cong \frac{\partial A}{\partial \omega} n^4 \tag{9}$$

Stix (1962) gives

$$S = 1 - \Sigma_{\pm} \frac{\omega_p^{\pm 2}}{(\omega^2 - \Omega_c^{\pm 2})} \cong 1 - \frac{\omega_{pe}^2}{\omega^2 - \Omega_c^2} \tag{10}$$

and

$$P = 1 - \Sigma_{\pm} \frac{\omega_p^{\pm 2}}{\omega^2} \cong 1 - \frac{\omega_{pe}^2}{\omega^2} \tag{11}$$

since ion effects are excluded. When Equations (10) and (11) are combined with Equations (2b) and (9), the result is

$$\frac{\partial A}{\partial \omega} = \frac{2\omega \, \omega_{pe}^2}{(\omega^2 - \Omega_{ce}^2)^2} \sin^2 \theta + \frac{2\omega_{pe}^2}{\omega^3} \cos^2 \theta \tag{12}$$

For near resonance cone propagation,

$$\tan^2 \theta \approx -\frac{P}{S} \tag{13}$$

implying

$$\cos^2 \theta \approx \frac{S}{S-P} \qquad (14)$$

and

$$\sin^2 \theta \approx \frac{P}{P-S} \qquad (15)$$

If these expressions are substituted into Equation (12), the result is

$$\frac{\partial A}{\partial \omega} = \frac{2(2\omega^2 - \Omega_{ce}^2 - \omega_{pe}^2)}{\omega(\omega^2 - \Omega_{ce}^2)} \qquad (16)$$

If $\Omega_{ce}^2 \gg \omega_{pe}^2 > \omega^2$, as usually occurs for nightside auroral hiss, then

$$\frac{\partial A}{\partial \omega} \approx \frac{2}{\omega} \qquad (17)$$

is an adequate approximation, and

$$\frac{\partial D^{(0)}}{\partial \omega} \approx \frac{2n^4}{\omega} \qquad (18)$$

It will be seen that Equation (18) usually gives results good to within an error of about 5% for reasonable values of ω, ω_{pe}, and Ω_{ce} when compared with numerically computed values of $\partial D^{(0)}/\partial \omega$. The frequency conditions cited after Equation (16) are usually good for nightside auroral hiss. On the dayside, ω_{pe}^2 is usually greater than Ω_{ce}^2.

Equation (18) allows Equation (7) to be even further simplified:

$$\gamma = \frac{4\pi^2 \omega \omega_{pe}^2}{k^2|\cos\theta|} \int_0^\infty v_\perp dv_\perp J_m^2 \left[\frac{\partial F^\pm}{\partial v_\perp} \frac{m\Omega_{ce}}{k} + \frac{\partial F^\pm}{\partial v_\|} \cos\theta\right] \qquad (19)$$

We are, in this work, concerned only with the Landau resonance, $m = 0$, since cyclotron resonances would involve relativistic resonance energies well above the range of HAPI. Intensities of electrons at relativistic energies are generally believed to be very low. With $m = 0$, Equation (19) reduces to

$$\gamma = \frac{4\pi^2 \omega_{pe}^2 \omega}{k^2|\cos\theta|} \int_0^\infty dv_\perp J_0^2 v_\perp \frac{\partial F}{\partial v_\|} \cos\theta \qquad (20)$$

It will be noted in a discussion of distribution functions that the approximation of a distribution symmetric in pitch angle appears to be a reasonable approximation at higher energies, where our most important calculations must be done. If this assumption is applied to Equation (20), along with the assumption that

$$\left|\frac{k_\perp v_\perp}{\Omega_{ce}}\right| \ll 1 \qquad (21)$$

where the distribution function F is large, an exceedingly simple and useful expression results. The latter assumption leads to $J_0^2 \approx 1$. The former assumption gives

$$v_\perp \frac{\partial F}{\partial v_\|} = v_\perp \frac{\partial F}{\partial E} \frac{\partial E}{\partial v_\|} = v_\perp \frac{\partial F}{\partial E} mv_\| = v_\| \frac{\partial F}{\partial E} \frac{\partial E}{\partial v_\perp} = v_\| \frac{\partial F}{\partial v_\perp} \qquad (22)$$

Equation (20) can then be integrated to give the result that

$$\gamma = \frac{-4\pi^2 \; \omega \; \omega_{pe}^2}{k^2} \; \text{sgn}(\cos \theta) \; v_\parallel \; F(v_\parallel) \tag{23}$$

where $v_\parallel$ is given by the Landau resonance condition, $v_\parallel = \omega/k_\parallel$. This condition can be used to eliminate the magnitude of the propagation vector k from Equation (23) to yield

$$\gamma = \frac{-4\pi^2}{\omega} \; \omega_{pe}^2 \; \text{sgn}(\cos \theta) \; v_\parallel^3 \; \cos^2\theta \; F(v_\parallel) \tag{24}$$

A final simplification occurs because the distribution function F from Kennel's derivation is normalized by the electron density, whereas the distribution function data received from the HAPI instrument is an absolute distribution function in units of particles s^3/km^6. The distribution function as detected by the HAPI instrument is here denoted by $\mathscr{F} = nF$. In SI units, $\omega_{pe}^2 = n_e^2/\epsilon_0 m_e = 3.183 \times 10^3 \; n(/m^3) \; (cycles/s)^2$. Thus,

$$\gamma = \frac{-4\pi^2 \times 3.2 \times 10^3}{\omega \times 1 \times 10^{18}} \; \text{sgn}(\cos \theta) \; \cos^2\theta \; v_\parallel^3 \mathscr{F}(v_\parallel) \tag{25}$$

where the division by 10^{18} is to convert from kilometers to meters in the distribution function. Multiplying out all numerical constants leaves a very simple formula for the linear growth rate due to the Landau resonance:

$$\gamma = \frac{-1.257 \times 10^{-13}}{\omega} \, \text{sgn}(\cos \theta) \, \cos^2\theta \, v_\|^3 \, \mathscr{F}(v_\|) \tag{26}$$

Note that the linear growth rate is negative, which indicates damping. The fact that growth is not possible according to this formula is due to the assumption of a spherically symmetrical distribution function. Since auroral hiss propagates close to the resonance cone, $\cos \theta$ can easily be estimated. Equations (10), (11), and (14) together yield

$$\cos^2 \theta \approx \frac{\omega^2(\Omega_{ce}^2 + \omega_{pe}^2 - \omega^2)}{\omega_{pe}^2 \, \Omega_{ce}^2} \tag{27}$$

Using the "nightside hiss" condition, $\Omega_{ce}^2 \gg \omega_{pe}^2 > \omega^2$, it is found that

$$\cos^2 \theta \propto \frac{\omega^2}{\omega_{pe}^2} \tag{28}$$

Equation (26) then yields

$$\gamma \propto -\omega \tag{29}$$

for a given resonant energy and distribution function.

In order to establish the essential correctness of the approximation (26), we will compare it with results computed numerically from Equation (20). Since Equation (20) and Equation (26) include either values or derivatives of the distribution function, we digress here to discuss how the distribution functions are dealt with.

If we look at the electron spectrograms for auroral hiss events shown in Figures 1 through 4, a pattern of electron excitation emerges. Over the polar cap, electron energies are low, with the distribution function getting close to zero between 1 and 10 keV. In the auroral zone, the electrons are more energetic and can change on time scales of less than a minute. Equatorward of the auroral zone, the electron distribution function is not as temporally varying as the auroral zone distribution function. The equatorward distribution function does go to higher energies than the polar cap distribution function. These electrons are usually thought to be in the plasma sheet. Because the objective of this work is not to model exactly any particular event in detail, but rather to extract a general result concerning the propagation and attenuation of auroral hiss, we take a representative event and compute some characteristic distribution functions over fairly extended time. However, before proceeding, it is interesting to simply look at some contour plots of distribution functions in the three regions of interest. The sample event is that of October 5, 1981, chosen because the auroral zone distribution function is not highly dynamic compared to other events and because it exhibits both attenuation and propagation equatorward of the source region.

Figures 5, 6, and 7 show contour plots of the electron distribution functions at 0400, 0412, and 0417 UT, respectively. These three distribution functions represent the distribution function as it is found in the polar cap, in the auroral zone where the electrons reach a maximum energy, and in the plasma sheet, respectively. Over the polar cap, propagation without attenuation is virtually always observed. The

distribution function displayed in Figure 5 is low energy and isotropic with no loss cone visible. Figure 6 shows the distribution function at a point toward the equatorward side of the auroral zone. This particular time is interesting because the electron distribution goes through a maximum in particle energy, according to Figure 3. The auroral hiss appears to undergo attenuation coincident with the spacecraft passage through this increase in the electron distribution. The values of the distribution function are visibly higher throughout the plot than those for the polar cap distribution. Another difference between the two distributions is that the loss cone is clearly visible at lower energies in the auroral zone distribution function. Even so, this distribution function is on the whole spherically symmetric. Figure 7 shows the distribution function of the plasma sheet electrons. This distribution appears to be less energetic than the auroral zone distribution function, except that values of the distribution function at high energies are maintained. The loss cone is again not distinguishable.

The contour plots just shown do not reflect the variation of the actual measurements made by the HAPI instrument because they are deliberately smoothed. Examination of the angle dependency of the measurements reveals a high level of fluctuation in the data. In particular, at high energies ($\geq$ 1 keV in the polar cap, $\geq$ 10 keV in the plasma sheet) the count rates become quite low, and the variation of the measured distribution function is of the same size as the measurements. At these energies, the loss cone is difficult if not impossible to pick out and the variation of the distribution function appears to be random. Except for the loss cone, it is unlikely that

the large fluctuations are due to real variation in the distribution function. It will be shown that the effect of a loss cone on the quantities we are calculating is minimal. Thus it makes sense to average the distribution function over pitch angle.

Each distribution function to be used must be processed from the data stored at Southwest Research Institute in San Antonio, Texas. Table 2 shows one form in which electron distribution function data comes from SwRI. This table represents one sweep through the energy range of the particle detector. The energy is stepped once every 15 ms. In this work, each distribution function sample is based on data taken during four consecutive spins of the spacecraft. Usually, four spins are equivalent in time to 54 energy sweeps, although in at least one early case, 26 energy sweeps were equivalent to four spins. Each set of the correct number of sweeps is sorted according to energy and ordered according to pitch angle. Table 3 shows the result of this operation for 7.4-keV electrons. Each sample distribution function consists of one table like this for each energy detected. Every such table gives the distribution function at the given energy as a function of pitch angle. These distribution function tables can be used in several ways to compute the growth rate. The general approach taken in this work is to average over pitch angle and to treat the distribution function as if it were spherically symmetric.

Time and angle averaged distribution functions for a polar cap and a plasma sheet distribution function for the October 5, 1981, event are shown in Figures 8 and 9 plotted in log-log form. The auroral zone distribution function is quite similar to the

plasma sheet distribution and is not shown here. The fact that these plots have regimes in which the distribution function versus energy gives roughly a straight line indicates that this portion of the distribution function can be thought of as a power law. This is, of course, an oversimplification. A cursory glance at these plots reveals several different regimes. For the data set chosen, the polar cap distribution function goes to zero at around 5 keV and recovers to nonzero values around 13 keV. It is normal for distributions over the polar cap to go abruptly to zero. The plasma sheet distribution displays a distinct high energy tail above 1.5 keV. This type of distribution is not unusual. In order to have idealized functions to deal with, a fit has been taken of the points seen to lie on a straight line. This operation yields the result that the distribution functions are given by

$$\mathcal{F}(E) = \frac{1.057 \times 10^6}{[E(eV)]^{2.619}} \left[\frac{sec^3}{km^6} \right] \tag{30a}$$

for the polar cap distribution function, and

$$\mathcal{F}(E) = \frac{5.408 \times 10^6}{[E(eV)]^{2.632}} \left[\frac{sec^3}{km^6} \right] \tag{30b}$$

for the plasma sheet distribution function. The plasma sheet distribution function will be used to test the method of computing the growth rate developed in this section.

In order to demonstrate the essential correctness of Equation (26), the value of γ is calculated in several ways. In order to do these calculations, use is made of ray

tracing results that will be explained in the next section. We will compare the results of Equation (26) with the results of numerically integrating Equation (20) for the power law (30b) and for that power law with a loss cone.

The method of computing γ to be tested is to use Equation (26) with a pitch-angle-averaged distribution function. This method is exceedingly simple, requiring the computation of no derivatives. The distribution function enters the computation only as $\mathscr{F}(0, v_{\parallel})$, the value of the spherically symmetric distribution function at the resonance energy. This requires simply taking the value of the distribution function at the resonance energy. In doing this, we lose information on the angular variation of the distribution function and the weighting function $J_0^2(k_{\perp} v_{\perp}/\Omega_{ce})$. However, as has been stated, the angular variation of the detected distribution function at large E is largely due to low count rates except for the loss cone. It will be seen that the square of the Bessel function is close to 1 where the distribution function is large.

We compare this method to that of using Equation (20), the full resonance cone approximated integral for $m = 0$, with the derived power law distribution function. One hundred points are taken between $v_{\perp} = 0$ and a point where the value of the integrand is very small compared to its largest value. In this case, the value was determined to be $v_{\perp} = 1.5 \times 10^8$ m/s. Simpson's rule was used to integrate over each triplet of points. Figure 10 shows values of the derivative for a sample position along a ray path taken at different beam energies. Note that as the beam energy, and therefore the resonant velocity, gets larger, the importance of the high energy tail is

relatively increased. Note, however, in Figure 11, that as the resonant velocity gets larger, the range in values in which J_0^2 is close to 1 is also expanded. Thus this approximation is good for all energies shown.

Figure 12 shows $d\mathscr{F}/dv_\parallel$ for the same set of parameters but with a loss cone folded into the distribution function. At $R/R_e = 2.5$ and $\lambda_{INV} = 70°$, where the source of the rays of this trial is placed, the loss cone is about 7°. To exaggerate the effect and to use a round number, a value of 10° is chosen. The effect on values of $d\mathscr{F}/dv_\parallel$ is shown in Figure 12. As can be seen, the only effect is at very small values of $v_\perp$, where the effect on the value of the growth rate is expected to be small. This is because of the factor of $v_\perp$ in the integrand of expression (20).

Results of these three methods of calculating γ are shown in Table 6. It can be seen that the three methods yield very similar results. Thus we conclude that Equation (26) ought to be a good method of calculating γ at high resonance energies. This method will be used in Section V to compute values of γ from Equation (26) using interpolated values of $\mathscr{F}(v_\parallel)$ from a table of distribution function versus energy.

A word about the effect of spacecraft charging is in order. It is well known that a conducting spacecraft in a plasma environment can charge negative (due to particle impacts) or positive (due to photoionization if it is in sunlight). Thus the spacecraft has a nonzero potential Φ_{sc} which affects the arrival energy of any particle detected at the spacecraft. If a particle is measured by the detector at kinetic energy E, the energy of the particle before it reached the spacecraft was $E + \Phi_{sc}$. Thus, to correct the distribu-

tion function for the effect of spacecraft charging, all that is necessary is to add Φ_{sc} to the detector energies, since the distribution function values remain the same. This can be formalized as a corollary of Liouville's Theorem (see Garrett, 1980)

$$F(v) = F(v')$$ (31)

where v and v' are two different particle velocities along the particle trajectory.

There is no exact procedure for determining Φ_{sc}. The spacecraft potential is indicated in most particle spectra by a sharp transition in the behavior of the distribution function. It is always found that Φ_{sc} is less than 20 eV for cases examined in this study. Since the resonance energies of interest in this work were found to be greater than or approximately equal to 1 keV, the spacecraft potential has only a minor effect on the computed value of the growth rate. Since the energy of the electron beam that is believed to generate the auroral hiss is not fixed by any observation, and the electron resonance energies are determined by the energy of the generating electron beam, we conclude that the spacecraft potential is unimportant for the conclusions of this thesis.

Once the linear growth rate has been computed, it is necessary to integrate the growth rate along the path to give the total growth (or damping). This is accomplished by computing the integral

$$\Gamma = \int_{path} \frac{\gamma}{V_g} \, ds$$ (32)

where Γ is the integrated growth rate, γ the growth rate at a given point, V_g the group velocity at a given point on the ray path, and the integral is taken along the calculated

ray path. The integral is done using a trapezoidal integral formula for the various points calculated along the ray path. The integrated growth rate Γ can be interpreted as follows. If the magnitude of the wave electric field at the beginning of the ray is E_0, then the magnitude at point A along the path is given by

$$E_A = E_0 e^\Gamma \tag{33}$$

This means that the change in the power of the noise is given by

$$\frac{P(A)}{P(r_0)} = e^{2\Gamma} \tag{34}$$

along the length of the ray. Thus, small changes in the value of Γ translate into large changes in the intensity of the auroral hiss.

CHAPTER IV. RAY PATHS

The calculation of the attenuation of auroral hiss due to Landau damping requires a calculation of the growth rate γ along the ray path. Since the growth rate cannot be calculated without knowledge of the ray path, we here describe a technique for evaluating the ray path.

The most general method of ray tracing uses the Haselgrove equations, the wave analogs of Hamilton's equations. This method was not chosen for this work because it has computational problems for rays propagating near the resonance cone. Since this is precisely the regime in which we are interested and since the present work does not require an extremely high degree of accuracy, we have chosen a very simple ray tracing scheme.

The ray tracing scheme we have chosen is a method known as Poeverlein's construction. An account of it is given in many books on plasma waves, e.g., that by Budden (1985). Poeverlein's construction uses two simple principals: Snell's law, and the fact that the path of a ray is normal to the index of refraction surface. For simplicity, the medium is treated as two dimensional and only propagation in the magnetic meridian plane is considered.

Poeverlein's construction uses two equations corresponding to the two principles previously stated. In geometric conditions such as those just stated, Snell's law reduces

to the statement that the component $n_\perp$ remains constant as the ray propagates. The cold plasma dispersion relation is given by Equations (2), (2a), and (2b) in the previous chapter. The quantities R, L, P, and S are the usual cold plasma parameters, also defined by Stix and displayed in Section I.

By utilizing the definitions $n_\perp = n \sin \theta$ and $n_\parallel = n \cos \theta$, the dispersion relation Equation (2c) is easily put into a quadratic form that can be solved for $n_\parallel$:

$$Pn_\parallel^4 + [(P + S)n_\perp^2 - 2PS]n_\parallel^2 + [Sn_\perp^4 - RLn_\perp^2 + PRL] = 0 \qquad (35)$$

If the position in space is known, then R, L, P, and S are calculable as functions of ω, ω_{pe}, and Ω_{ce}. The value of $n_\perp$ is known from the launch condition of the ray. It is a matter of solving a quadratic equation to find $n_\parallel$. Thus, at any given position, the index of refraction and wave normal angle can be calculated.

But how does one compute the position? To step the position in space from the launch position, Equation (35) is differentiated to give the normal to the index of refraction surface. If ψ is the ray path angle to the magnetic field, differentiation of Equation (32) results in

$$\tan \psi = \frac{dn_\parallel}{dn_\perp} = \frac{-(S + P)n_\perp n_\parallel^2 - 2Sn_\perp^3 + RLn_\perp}{2Pn_\parallel^3 + [(S + P)n_\perp^2 - 2PS]n_\parallel} \qquad (36)$$

It should be noted that the right side of Equation (36) is antisymmetric in both $n_\perp$ and $n_\parallel$. A step size must be chosen to advance the ray in the calculated direction.

The question remains how to launch the ray. The assumption used here is that the auroral hiss is generated by an electron beam at energy E_b in the Landau resonance. The condition for the Landau resonance is

$$v_b = \frac{\omega}{k_|} \tag{37}$$

where $v_b = 2E_b/m_e$. Since $k_| = (n\omega/c) \cos \theta$, this equation reduces to

$$\frac{v_b}{c} = \frac{1}{(n \cos \theta)} = \frac{1}{n_|} \tag{38}$$

With the value of $n_|$ determined by the beam energy, the initial value of $n_\perp$ can be found from Equation (35).

The ray tracing procedure can be summed up as follows. Figure 13 gives a pictorial representation of the various steps of the procedure. A source position and a generating beam energy are chosen. At the starting position, position A in Figure 13a, ω_{pe} and Ω_{ce} are calculated, leading to values for cold plasma parameters R, L, P, and S. These values of the cold plasma parameters are put into Equation (35) to give the curve labeled α in Figure 13b. Equation (35) is then solved for $n_\perp$. Thus $n_\perp$ and $n_|$ are known for the starting position. This point is labeled A' in Figure 13b. The ray direction is the perpendicular to the index of refraction direction and is given by the arrow emerging from point A'. This direction is calculated from Equation (36). The ray is stepped in the direction indicated by the arrow. At this new position, R, L, P, and S are calculated anew. Thus, using Equation (35), curve β can be computed. The

line η is a line of constant $n_\perp$ and goes through point A'. The next index of refraction point, B', is the point where curves η and β intersect. Point B' gives the new value of $n_\parallel$, the value of $n_\perp$ remaining the same. The value of $n_\parallel$ can be found analytically by solving Equation (35) for $n_\parallel$. The arrow at point B' gives the direction from point B to point C in Figure 13a. This direction is again given analytically by Equation (36). At point C, the electron plasma and cyclotron frequencies can be recalculated, leading to new values of the cold plasma parameters. From these values, curve γ can be computed. The intersection of η with γ gives the new value of $n_\parallel$, and the arrow at this point, C', gives the direction from point C to point D in Figure 13a, and so on. All of these operations are done analytically, curves being shown here for illustrative purposes only.

Another quantity which it is necessary to get out of the ray tracing procedure is the group velocity V_g. The definition of group velocity is given by

$$V_g = \frac{\partial \omega}{\partial k} \tag{39}$$

This quantity is straightforward, if somewhat tedious, to compute from the dispersion relation (35). By making use of the relation $n = ck/\omega$, differentiating with respect to $k_\perp$ and $k_\parallel$, and solving for $\partial \omega / \partial k_\perp$ and $\partial \omega / \partial k_\parallel$, the following equations are found:

$$\frac{\partial \omega}{\partial k_\perp} = \frac{2RL(\frac{c}{\omega})^2 k_\perp - 2(P+S)(\frac{c}{\omega})^4 k_\parallel^2 k_\perp - 4S(\frac{c}{\omega})^4 k_\perp^3}{\frac{\partial}{\partial \omega}[(\frac{c}{\omega})^4 P] k_\parallel^4 + \frac{\partial}{\partial \omega}[(P+S)(\frac{c}{\omega})^4] k_\perp^2 k_\parallel^2 - 2\frac{\partial}{\partial \omega}[PS(\frac{c}{\omega})^2] k_\parallel^2 + \frac{\partial}{\partial \omega}[S(\frac{c}{\omega})^4] k_\perp^4 - \frac{\partial}{\partial \omega}[RL+PS](\frac{c}{\omega})^2 k_\perp^2 + \frac{\partial(PRL)}{\partial \omega}}$$

(40a)

$$\frac{\partial \omega}{\partial k_\parallel} = \frac{-4(\frac{c}{\omega})^4 P k_\parallel^3 - 2[(P+S)(\frac{c}{\omega})^2 k_\perp^2 - 2PS](\frac{c}{\omega})^2 k_\parallel}{\frac{\partial}{\partial \omega}[(\frac{c}{\omega})^4 P] k_\parallel^4 + \frac{\partial}{\partial \omega}[(P+S)(\frac{c}{\omega})^4] k_\perp^2 k_\parallel^2 - 2\frac{\partial}{\partial \omega}[PS(\frac{c}{\omega})^2] k_\parallel^2 + \frac{\partial}{\partial \omega}[S(\frac{c}{\omega})^4] k_\perp^4 - \frac{\partial}{\partial \omega}[RL+PS](\frac{c}{\omega})^2 k_\perp^2 + \frac{\partial(PRL)}{\partial \omega}}$$

(40b)

Since the cold plasma parameters are functions of ω only, the derivatives given in the above formulas can be calculated analytically. Thus V_g can be computed exactly within the limits of the model. In all calculations the computed values of the components of V_g are used to compute the value of ψ. This value of ψ is compared with the value computed from Equation (36). In all cases the two values agree exactly, indicating that the two formulas are analytically the same, as indeed they should be.

A word should be said about the magnetic field and plasma density models that were used in this calculation. The magnetic field is computed from a standard Earth-centered dipole model of strength 3.1×10^{-5} Tesla at the magnetic equator at the Earth's surface. The electron density is estimated from the auroral hiss high frequency cutoff and is assumed constant. Another possibility is the model of Persoon et al. (1983), which gives an altitude dependence of

$$n_e \propto \frac{1}{R^{3.85}} \tag{41}$$

but this is a statistical relation which does not necessarily apply in individual cases. Since the path lengths that will be dealt with here are less than an Earth radius, variations in the plasma density are believed to be relatively unimportant. Since there is no way to measure the spatial variation of the plasma density away from the spacecraft, a single representative density over the duration of a given event has been assumed.

There are two important limitations of the ray tracing scheme presented here. First, the scheme as presented is strictly a procedure for determination of propagation characteristics in the magnetic meridian plane. We are not able to discuss east--west propagation. Second, the ray tracing scheme assumes variation of the plasma and cyclotron frequencies in the magnetic field direction only. Thus, it is impossible to assess the effect of transverse plasma density gradients, for example, for a ray entering the plasmapause. Also, the assumption has been made that the gradient of the magnitude of the magnetic field is along the magnetic field direction. This assumption introduces an error which must now be assessed.

To assess the error due to assuming that $\nabla|\mathbf{B}|$ is parallel to $\mathbf{B}$, the dipole field model is used to compute the directions of $\mathbf{B}$ and $\nabla|\mathbf{B}|$. The angle between these two vectors is given by

$$\delta = \tan^{-1}\left(\frac{1}{2}\tan\theta\right) - \tan^{-1}\left[\frac{\cos\theta\,\sin\theta}{1 + 3\cos^2\theta}\right] \qquad (42)$$

Sample indexes of refraction are shown in Figure 14 for a ray starting at $R = 2.5\,R_e$ and $\lambda_{INV} = 70°$, a plausible auroral zone source point. The Persoon et al. (1983) density law (41) is incorporated to exaggerate the differences between the index of refraction curves along the ray path, as shown in the figure. The lines of constant $|\mathbf{B}|$ are shown in the figure to express graphically where the values of $n_\perp$ and $n_\parallel$ would be plotted if the ray tracing were done correctly. In this case, the component of the index of refraction perpendicular to the lines of constant $|\mathbf{B}|$ would be conserved. It can be seen from Figure 14 that this leads to an error of less than 5% in either component of $\mathbf{n}$. Because all of the rays traced are well out on the resonance cone, this error estimate applies to all energies. Because the model utilized in the next section assumes constant density, the error due to this effect is negligible since the index of refraction surface changes very little over the path of the ray. The question of the tilt of the surface of constant $|\mathbf{B}|$ with respect to the magnetic field will have its greatest effect when the resonance cone angle is changing rapidly over the ray path or when the index of refraction surface becomes nearly parallel to the direction of stratification. These conditions do not occur in the model ray tracings to be discussed since they are confined to small path lengths and neither the electron plasma frequency nor the electron cyclotron frequency are approached.

It should also be noted that the effect of the tilt of the surface of constant $|\mathbf{B}|$ with respect to the magnetic field will have very little effect on the tracing of the ray position. Because all rays traced are very close to the resonance cone, the ray direction is always virtually perpendicular to the resonance cone. Thus the error in ray direction due to the slight displacement of the value of $\mathbf{n}$ is virtually nil.

CHAPTER V. COMPARISON WITH OBSERVATIONS

In this section, all of the techniques discussed in the previous sections will be used to discuss a test case of auroral hiss propagation and damping. The distribution functions used are the average distribution functions displayed in Tables 4 and 5 and in Figures 8 and 9. We will assume a likely auroral hiss source location at $R = 2.5$ R_e and $\lambda_{INV} = 70°$. Ray tracing will be done assuming a constant plasma frequency of 20 kHz and the usual magnetic dipole moment of 3.1×10^{-5} Tesla R_e^3. Starting at the source point, each ray will be traced until it reaches a point 2.5° INV away from the source invariant latitude.

It is important to point out again the limitations of this approach and how they apply in the present case. The ray tracing approach adopted here does not include the possibility of density variation in the direction perpendicular to the magnetic field. This precludes taking into account phenomena like density cavities (see Persoon et al., 1986) or the plasmapause, two important phenomena that might have an effect on the propagation of the auroral hiss waves. The source region for the auroral hiss is in fact in the same region as the observed density cavities, and it may be that the auroral hiss that we observe is generated in a region of reduced density. The rays traced here should be taken as a modeling of the auroral hiss propagation outside of the auroral zone and away from the observed density cavities. Thus, what is cited as a beam

energy is more accurately thought of as the resonance energy at the point that we start tracing the ray. This resonance energy evolves somewhat during the transit of the wave. Since we know the frequency of the wave, the resonance energy translates into the propagation vector or wavelength of the auroral hiss. The main result of this section will be to put limits on the wavelength of auroral hiss.

At this point it is good to remember some of the limitations of the distribution function models used. The fact that the distribution function is angle averaged has been shown to have a negligible effect. The fact that it is time averaged, however, means that we are not actually measuring the time variation in the damping. This is not an important consideration over the polar cap since the distribution is cold and quiet there. However, equatorward of the source region, in the auroral zone, the distribution function is very dynamic. The distribution function chosen as a sample in the equatorward direction does not take into account temporal variation in the auroral zone but rather is an average over quiet but relatively energetic plasma sheet electrons. Thus, we are extracting an average result for damping equatorward of the auroral zone.

Figure 15 shows the results of ray tracing at five different "beam energies" under the conditions given in the introduction to this section. The energies used are 0.1, .32, 1.0, 3.2, and 10.0 keV. Note that the paths of the rays are indistinguishable on the scale plotted. The reason for this is that all beam energies give solutions for the index of refraction vector that are close to the resonance cone. Thus changing the

energy changes the angle of propagation only very slightly. For our purposes, these ray paths are the same.

Figure 16 gives results for the growth rate γ as the ray propagates along the poleward ray path. These values of γ are calculated from Equation (26) using the distribution function given in Table 4. These results show that, given the assumption of generation by a beam, the energy of the beam has a tremendous effect on the damping rate. Damping for a 0.1 keV beam is over 700/s, while for a 10 keV generating beam the damping is essentially 0.

Figure 17 shows the result of integrating the results shown in Figure 16 over the path length according to Equation (32). Here they are plotted as a function of invariant latitude. This figure shows that, for propagation over a range in invariant latitude of 2.5°, only auroral hiss generated by the two highest beam energies is at all viable. In fact, utilizing Equation (34), we find that the auroral hiss power generated by a 3.2 keV beam must fall off in power by a factor of 7. From looking at the spectrograms shown in Figures 1 through 4, which are typical in terms of auroral hiss attenuation, it is clear that attenuation by an order of magnitude is not usually observed in poleward propagating auroral hiss within 2.5 ° INV of the source. The result of this computation implies that if the auroral hiss is generated by an electron beam, then that beam is of energy greater than 3.2 keV. This effectively puts a limit on $k_{\parallel}$, once the wave has propagated out of the source region. The value of $k_{\parallel}$ is 3.7×10^{-3}/m with $\theta \approx 1$ rad, λ is found to be 2 km.

Figure 18 shows the growth rate calculated for the equatorward ray path at the same five energies as for the poleward case. Two differences between the poleward and equatorward cases are apparent. First, the values of the damping coefficient in the equatorward direction are much larger than for the poleward case. Second, the highest energy does not give the lowest damping, as with the poleward case. A glance at Figure 8 indicates why this is the case. The distribution function has a high energy tail that maintains the value of F at a roughly constant value while $v_\parallel$ becomes larger. Thus the value of the damping coefficient (that is $-\gamma$) grows as the beam energy gets larger.

Figure 19 shows the variation of the integrated growth rate with invariant latitude. The lowest integrated damping is that for the 1 keV electron beam. The integrated damping coefficient after propagating through 2.5° INV is about -20, giving a fall off in power of 2×10^{17}. This result indicates that the auroral hiss should be completely damped almost immediately after it is generated. Values of $k_\parallel$ for the 10 keV beam are about 2.0×10^{-3}/m with $\theta \approx 1$ rad, λ is found to be > 3 km.

These calculations were done using the actual angle averaged electron distributions displayed in Tables 4 and 5 and in Figures 7 and 8. Thus, in a general way, the difference in poleward and equatorward intensity can be attributed to the high energy tail in the equatorward distribution function seen from about 1.5 keV up. However, the fact that auroral hiss is often observed propagating through the plasma sheet seems to indicate that the damping is not as effective as calculated here.

It is of interest to examine the effect of frequency on the damping of auroral hiss. Figure 20 shows some rays traced to end at the end points reached in Figure 14 but beginning at different points along the $\lambda_{INV} = 70°$ field line. They are labelled to indicate the frequency. In the approximation that we are using, ω_{pe} does not change along the path of the ray. It is easy to imagine the rays in this diagram as straight lines. Then the path length follows the relation

$$\Delta s \propto \frac{1}{\sin \psi} \approx \frac{1}{\cos \theta} \approx \frac{1}{\cos \theta_{Res}}$$

Combining this statement with relations (28), (29), and (32) yields

$$\Gamma = \int \frac{\gamma}{V_g} ds \propto \cos \theta_{Res} \frac{1}{V_g} \times \frac{1}{\cos \theta_{Res}}$$

To a zeroth order approximation,

$$\Gamma \propto \frac{1}{V_g(\omega)} \tag{43}$$

Unfortunately, we have no simple expression for V_g near the resonance cone. Expression (43) gives the zeroth order dependence of the integrated growth rate on a frequency for Landau damped auroral hiss. Some results are calculated and displayed in Figure 21 for γ and Figure 22 for Γ. It can be seen in Figure 21 that $\gamma \sim \omega$ and the pathlength $\Delta s \sim 1/\omega$. Figure 22 shows that higher frequency implies higher damping, although no simple proportionality is evident. Equatorward tracing gives a similar result and is not shown. According to these results, for a point source of

auroral hiss, higher frequency waves ought to be damped out before lower frequency waves. In fact, we see something like this in Figure 2 around 65° INV where the auroral hiss appears to have a sharply descending intensity drop. This is somewhat obscured by an increase in auroral hiss intensity that appears to be due to another source. Other events with upper cutoffs of this type have been observed, mostly on the nightside. On the other hand, the attenuation in Figure 3 at 67° INV appears to be constant across the bandwidth of the auroral hiss. This could be because the downward slope of the intensity profile is too sharp to be resolved by the 32 s sweep time of the PWI instrument or because the attenuation is caused by another effect, such as reflection due to a density boundary. Examination of the faint auroral hiss equatorward of this point reveals a hint of a downward sloping intensity profile. Although this intensity profile can be obscured by source geometry and other effects, the existence of this type of signature should be taken as an indication that Landau damping is occurring.

CHAPTER VI. CONCLUSIONS

The study in the previous section indicates that Landau damping is an important effect to be considered in the propagation of auroral hiss. Studies of the variation of damping with beam energy indicate that on the poleward side of the source, beam energies of 1 keV or greater are generally required to avoid significant damping. These beam energies correspond to wavelengths on the order of 2 km or greater. On the equatorward side, significant damping is always predicted for resonance energies of 10 keV or less. For auroral hiss to propagate equatorward with negligible damping, it must have wavelengths greater than 3 km.

These results lead to a question concerning the generation of auroral hiss, namely, where are the beams needed to generate upgoing auroral hiss at these resonance energies? Upgoing beams of several kilovolt energy are rarely visible in the particle data. As an example, a faint beam of about 7 keV has been detected on the poleward edge of the auroral zone during the October 5, 1981, event. Usually, however, the beam energy is on the order of a few hundred electron volt energy. According to the present calculations, auroral hiss from such beams should be heavily damped going in either direction. In a study by Lin et al. (1984) the existence of dayside auroral hiss has been correlated with the occurrence of 100 eV electron beams. No such correlation was found at keV beam energies.

It has been suggested that the observed equatorward attenuation of auroral hiss could be a temporal effect, for instance due to variation in the beam energy or intensity. It seems likely that temporal effects in auroral hiss do exist, a good example being the September 26, 1981 event in Figure 2. In this case, the poleward extension of the auroral hiss noise exhibits many abrupt fluctuations in intensity, which may very well be due to a variation in the strength of the generating beam. If this is the case, a fluctuation in beam energy could conceivably cause the observed equatorward attenuation as long as the beam energy never goes below resonance energies that would cause damping on the poleward side. However, given the generally consistent pattern of auroral hiss intensity decreasing in the equatorward directions, temporal effects are an unlikely explanation.

Thus, the results of Landau damping computations highlight some problems with the expected model of auroral hiss propagation. First, auroral hiss must be propagating at longer wavelengths than has previously been suggested. Waves generated at wavelengths shorter than about 2 km will be damped immediately, both poleward and equatorward of the source region. Second, however, long wavelength waves imply beams of higher energy than are generally seen. We now put forward some ideas about how this situation could occur.

1. The spacecraft is flying either east or west of the electron beam that generates auroral hiss. If the source of radiation is strictly a beam, then the observer should not expect to see it all or even most of the time. Noise created by a beam

would take the shape of a solid cone in space. The spacecraft should trace a line through this solid cone, and it would be only by coincidence that one could expect to observe the source beam of the hiss noise. In this scenario, the spacecraft, traveling north to south, passes either east or west of the source, and our assumption of north-south propagation is grossly incorrect near the source region.

The association of auroral hiss with auroral arcs makes it seem likely that the source of auroral hiss has a sheet-like geometry rather than a line-like geometry. The idea of sheet-like geometry for the source region is apparently confirmed by the observation that over the polar cap, the auroral hiss does not appear to fall off as $1/distance^2$. Instead, it appears to remain quite constant. It should be born in mind, however, that other explanations may account for this spatial variation and the association of auroral hiss with visible auroral arcs has been made only for downward propagating hiss. It is not at all clear that the upward propagating hiss dealt with here is associated with the same source region as for downward propagating auroral hiss.

2. The auroral hiss is actually generated by a high energy component of the beam which is completely dissipated before reaching the spacecraft. This appears unlikely since Lin et al. (1984) have calculated the most efficient generation to be at beam energies under 100 eV.

3. The generating beam is accelerated to high energy and then flows through a retarding potential so that we only see it at low energy.

Unfortunately, limitations in the altitude coverage of the HAPI data set do not allow us to explore possibilities 2 and 3 observationally.

4. The beam is at energies above the detection limit of HAPI (13 keV).

5. The beam is unnecessary and hiss can be generated by a mode conversion from some other mode of radiation. In fact, auroral hiss is almost always seen in company with broadband electrostatic noise. Unfortunately, the mode of broadband electrostatic noise has not been identified, so it is impossible at the present to give a meaningful assessment of the validity of this hypothesis. It may be that broadband electrostatic noise is not due to a propagating wave at all, but is simply the detector's response to the spacecraft traversing quasi-electrostatic fields. If this is true, then the broadband electrostatic noise may indicate the presence of static fields causing the acceleration of electron beams and, indirectly, auroral hiss. In regard to this hypothesis, it should be noted that sometimes radiation that looks like the higher frequency band of broadband electrostatic noise has a magnetic component. These emissions are likely to be whistler mode emissions close to the magnetic field line. If such emissions are generated at the Landau resonance, the existence of high energy electron beams is required.

6. Auroral hiss is transformed in wavelength by a partial transmission at a boundary in the index of refraction caused by an abrupt change in the plasma density. Because nightside density cavities, investigated by Persoon et al. (1986), are a well-known phenomenon, and data from the Viking spacecraft (Hilgers, 1992) seem to

confirm the idea that there is small scale structure in a density cavity, this idea is very plausible. For this reason, we will explore this concept somewhat more completely.

The idea of an abrupt wavelength conversion of whistler mode waves due to reflection and transmission across a field-aligned density irregularity is discussed by Bell and Ngo (1990). Their discussion is for whistler mode noise not far out on the resonance cone so that four possible modes must be accounted for. In adapting this idea to the present problem, there will be only two possible modes for each medium, since we are dealing only with propagation near the resonance cone.

The principle of this mechanism is the principle on which Poeverlein's construction is based: the component of the index of refraction parallel to the interface between two regions of differing index of refraction remains constant as a ray crosses the interface. This is Snell's Law. However, now instead of dealing with a gradual change while moving along the magnetic field direction, we are concerned with an abrupt change in the direction perpendicular to the magnetic field. The density irregularity can be considered to run either parallel or oblique to the magnetic field line. Then, the component of the index of refraction parallel to that interface stays constant as the ray passes through the interface.

Figure 23 illustrates how this mechanism might work. The density interface is assumed to be oblique to the magnetic field by an angle of $20°$. The difference between the two dispersion relations is caused by a 5% difference in density. The n_1' component is the component of the index of refraction parallel to the interface. As one

can see, if the interface were parallel to the magnetic field, the line of constant $n_\perp'$ would be equivalent to a line of constant $n_\perp$, and there would be only a change of direction of propagation from the partial transmission and reflection. Because of the obliquity of the line of constant $n_\perp'$, the wave is converted from a large index of refraction to a small index of refraction. The Cerenkov condition, Equation (37), implies that if $k_\parallel$ can be made smaller, the resonance velocity and therefore the resonance energy can be made larger. From this diagram, it is seen that an obliquity of 20° is enough to change $n_\parallel$ by a factor of about 3. Using Equation (37) and converting the resonance velocity into an energy gives a change in resonance energy of a factor of ~ 10. This means that hiss noise generated by a beam of energy 100 eV, a commonly observed beam energy, will be converted to hiss noise with electron resonance energy of 1000 eV if the wave passes through a density fluctuation oblique to the magnetic field by an angle of 20°.

Because the wave propagates perpendicular to the index of refraction surface, the newly created long wavelength waves are reflected back into the first medium, while the short wavelength wave that we require is transmitted into the new medium where it is quickly damped. However, a multiple reflection mechanism can easily be invoked to get the long wavelength wave going in the right direction. Such a mechanism is sketched in Figure 24. This figure shows index of refraction diagrams for two reflections of a whistler mode wave along with the path of the ray as it reflects from the walls of a density cavity oblique to the magnetic field. This diagram shows

that the second and subsequent even numbered transmitted rays will be of long wavelength and will be transmitted in the correct direction. On the other hand, the odd numbered transmitted rays will have wavelengths close to that of the initial ray. The existence of an oblique density cavity could be due to an oblique double layer. Oblique double layers are discussed by Borovsky and Joyce (1983).

Figure 25 explores an alternative situation in which the density cavity is flared outward in the upward direction. This scenario is attractive because each reflection has the effect of lengthening the wavelength and waves of the modified wavelength emerge from the density cavity in both directions. If a ray goes through a large number of reflections, it may be possible to modify the wavelength significantly with a small angle of obliquity of the cavity wall to the magnetic field.

In this thesis, a model of Landau damping has been presented. According to this model, a large difference has been calculated between damping of auroral hiss poleward and equatorward of the source region. This difference is more than enough to account for observed differences in auroral hiss intensity when the equatorward hiss is damped. In fact, it is somewhat difficult to account for cases where the equatorward auroral hiss propagates undamped for any distance. The observed unimpeded propagation must occur because of the long wavelength and consequently high resonance energy of the whistler mode waves. These waves must have resonance energies higher than particle energies detected by HAPI.

The importance of Landau damping has been explored in this paper, although we are unable to model particular cases exactly. The results of this work raise questions about the propagation of auroral hiss that are somewhat difficult to answer, although a number of possible solutions have been put forward in this section. In particular, a transmission--reflection mechanism using density cavities oblique to the magnetic field has been discussed as a possible method of changing the wavelength so that auroral hiss waves can propagate with acceptable attenuation. This mechanism, which involves density cavities running oblique to the magnetic field direction, provides a plausible method for converting short wavelength hiss to long wavelength auroral hiss.

Table 1. Relative Strength of Poleward and Equatorward Auroral Hiss

Comparison of Intensity	Number of Occurrences	Percentage of Occurrences
Equatorward > Poleward	5	4.8%
No difference	32	30.8%
Poleward > Equatorward	67	64.4%

Table 2. Sample Sweeps of HAPI Electron Distribution Function Data

```
         DISTRIBUTION FUNCTION

    IL            MLT          ALT(KM)     GEOD LAT     GEOD LONG
 6.925E+01     2.216E+01     1.360E+04    4.787E+01    -1.348E+02

    LST           L            ORBIT       DARK=0
 2.301E+01     7.964E+00     1.610E+02    1.000E+00

         ELECTRONS
```

HR	MIN	SEC	EV	PA	DET 0	DET 2	DET 4
7	54	0.69	1.321E+04	1.301E+02	0.000E+00	0.000E+00	0.000E+00
7	54	0.69	9.900E+03	1.309E+02	0.000E+00	0.000E+00	0.000E+00
7	54	0.69	7.425E+03	1.318E+02	1.472E-02	0.000E+00	0.000E+00
7	54	0.69	5.569E+03	1.327E+02	2.379E-02	0.000E+00	2.379E-02
7	54	0.69	4.188E+03	1.336E+02	0.000E+00	0.000E+00	3.850E-02
7	54	0.69	3.121E+03	1.344E+02	6.365E-02	0.000E+00	6.365E-02
7	54	0.69	2.339E+03	1.353E+02	3.150E-01	0.000E+00	3.150E-01
7	54	0.69	1.753E+03	1.362E+02	3.488E-01	0.000E+00	1.068E+00
7	54	0.69	1.319E+03	1.371E+02	1.014E+00	0.000E+00	1.014E+00
7	54	0.69	9.844E+02	1.380E+02	4.065E+00	0.000E+00	3.510E+00
7	54	0.69	7.387E+02	1.389E+02	6.893E+00	0.000E+00	9.400E+00
7	54	0.69	5.536E+02	1.398E+02	1.180E+01	0.000E+00	1.896E+01
7	54	0.69	4.168E+02	1.408E+02	2.508E+01	0.000E+00	2.386E+01
7	54	0.69	3.133E+02	1.417E+02	4.538E+01	0.000E+00	4.327E+01
7	54	0.69	2.346E+02	1.426E+02	4.148E+01	0.000E+00	4.886E+01
7	54	0.69	1.757E+02	1.435E+02	4.536E+01	0.000E+00	3.888E+01
7	54	0.69	1.320E+02	1.444E+02	0.000E+00	0.000E+00	0.000E+00
7	54	0.69	9.893E+01	1.453E+02	0.000E+00	0.000E+00	0.000E+00
7	54	0.69	7.419E+01	1.461E+02	0.000E+00	0.000E+00	1.064E+02
7	54	0.69	5.566E+01	1.470E+02	1.257E+02	0.000E+00	1.257E+02
7	54	0.69	4.191E+01	1.480E+02	2.211E+02	0.000E+00	0.000E+00
7	54	0.69	3.131E+01	1.489E+02	0.000E+00	0.000E+00	0.000E+00
7	54	0.69	2.357E+01	1.498E+02	4.621E+03	0.000E+00	9.241E+03
7	54	0.69	1.776E+01	1.507E+02	5.768E+04	0.000E+00	6.504E+04
7	54	0.69	1.346E+01	1.517E+02	1.751E+05	0.000E+00	1.922E+05

Table 3. Data From 54 Sweeps of Sample Data

E(eV)	α(degrees)	$\mathscr{F}(sec^3/km^6)$
7.412E+03	1.746E+02	0.000E+00
7.412E+03	1.735E+02	0.000E+00
7.412E+03	1.713E+02	0.000E+00
7.412E+03	1.690E+02	1.470E-02
7.412E+03	1.684E+02	0.000E+00
7.412E+03	1.623E+02	2.940E-02
7.412E+03	1.590E+02	0.000E+00
7.412E+03	1.525E+02	0.000E+00
7.412E+03	1.522E+02	1.470E-02
7.412E+03	1.494E+02	1.470E-02
7.412E+03	1.455E+02	2.210E-02
7.412E+03	1.426E+02	2.210E-02
7.412E+03	1.426E+02	1.470E-02
7.412E+03	1.355E+02	2.940E-02
7.412E+03	1.329E+02	1.470E-02
7.412E+03	1.261E+02	1.470E-02
7.412E+03	1.257E+02	2.210E-02
7.412E+03	1.231E+02	1.470E-02
7.412E+03	1.186E+02	1.470E-02
7.412E+03	1.162E+02	2.940E-02
7.412E+03	1.156E+02	2.940E-02
7.412E+03	1.084E+02	0.000E+00
7.412E+03	1.064E+02	2.210E-02
7.412E+03	9.970E+01	2.940E-02
7.412E+03	9.870E+01	0.000E+00
7.412E+03	9.680E+01	0.000E+00
7.412E+03	9.170E+01	1.470E-02
7.412E+03	8.990E+01	1.470E-02
7.412E+03	8.870E+01	0.000E+00
7.412E+03	8.180E+01	1.470E-02
7.412E+03	8.000E+01	1.470E-02
7.412E+03	7.320E+01	0.000E+00
7.412E+03	7.200E+01	2.940E-02
7.412E+03	7.020E+01	2.210E-02
7.412E+03	6.510E+01	1.470E-02
7.412E+03	6.310E+01	0.000E+00
7.412E+03	6.220E+01	0.000E+00
7.412E+03	5.530E+01	1.470E-02
7.412E+03	5.320E+01	1.470E-02
7.412E+03	4.620E+01	1.470E-02
7.412E+03	4.560E+01	1.470E-02
7.412E+03	4.340E+01	1.470E-02
7.412E+03	3.880E+01	1.470E-02
7.412E+03	3.640E+01	2.210E-02
7.412E+03	3.600E+01	3.680E-02
7.412E+03	2.920E+01	1.470E-02
7.412E+03	2.650E+01	1.470E-02
7.412E+03	1.980E+01	0.000E+00
7.412E+03	1.970E+01	1.470E-02
7.412E+03	1.710E+01	0.000E+00
7.412E+03	1.350E+01	2.210E-02
7.412E+03	1.100E+01	1.470E-02
7.412E+03	1.090E+01	0.000E+00
7.412E+03	7.300E+00	0.000E+00

Table 4. Angle and Time-Averaged Distribution Function,
October 5, 1981, Poleward of Source Region

E(eV)	$\mathscr{F}(\text{sec}^3/\text{km}^6)$
1.319E+04	1.464E-04
9.883E+03	0.000E+00
7.408E+03	0.000E+00
5.552E+03	1.664E-05
4.171E+03	7.387E-04
3.104E+03	5.523E-04
2.322E+03	1.424E-03
1.736E+03	2.623E-03
1.302E+03	1.904E-03
9.674E+02	1.405E-02
7.217E+02	2.112E-02
5.366E+02	1.167E-01
3.998E+02	2.174E-01
2.963E+02	7.347E-01
2.176E+02	1.490E+00
1.587E+02	3.731E+00
1.150E+02	5.034E+00
8.193E+01	8.382E+00
5.719E+01	2.762E+01
3.866E+01	5.816E+01
2.491E+01	1.908E+02
1.431E+01	6.305E+02
6.570E+00	1.812E+03
7.600E-01	4.344E+03

Table 5. Angle and Time-Averaged Distribution Function,
October 5, 1981, Equatorward of Source Region

E(eV)	$\mathscr{F}(sec^3/km^6)$
1.319E+04	9.484E-03
9.883E+03	8.461E-03
7.408E+03	1.093E-02
5.552E+03	1.458E-02
4.171E+03	1.327E-02
3.104E+03	1.252E-02
2.322E+03	1.936E-02
1.736E+03	1.452E-02
1.302E+03	2.467E-02
9.674E+02	6.814E-02
7.217E+02	1.810E-01
5.366E+02	4.478E-01
3.998E+02	1.074E+00
2.963E+02	2.339E+00
2.176E+02	3.898E+00
1.587E+02	7.617E+00
1.150E+02	1.795E+01
8.193E+01	4.070E+01
5.719E+01	1.038E+02
3.866E+01	3.844E+02
2.491E+01	1.418E+03
1.431E+01	4.431E+03
6.570E+00	1.177E+04
7.600E-01	2.477E+04

Table 6. Comparisons: Three Ways of Computing γ,
Two Ways of Computing $\partial D^{(0)}/\partial\omega$

E_b(keV)	$\gamma(s^{-1})$ Numerical	$\gamma(s^{-1})$ Numerical w/loss cone	$\gamma(s^{-1})$ Approximate	$\partial D^{(0)}/\partial\omega$ Numerical	$\partial D^{(0)}/\partial\omega$ Approximate
0.1	-3.262×10^3	-3.231×10^3	-3.290×10^3	3.315×10^3	3.154×10^3
.32	-8.698×10^2	-8.257×10^2	-8.809×10^2	3.225×10^2	3.075×10^2
1.0	-2.405×10^2	-2.287×10^2	-2.436×10^2	3.302×10^1	3.134×10^1
3.2	-6.488×10^1	-6.174×10^1	-6.573×10^1	3.186×10^0	3.020×10^0
10.0	-1.813×10^1	-1.725×10^1	-1.843×10^1	3.127×10^{-1}	2.963×10^{-1}

Figure 1.   Spectrogram of auroral hiss event on September 18, 1981.

DYNAMICS EXPLORER
JOINT DATA PRESENTATION

YR/DAY: 81/261
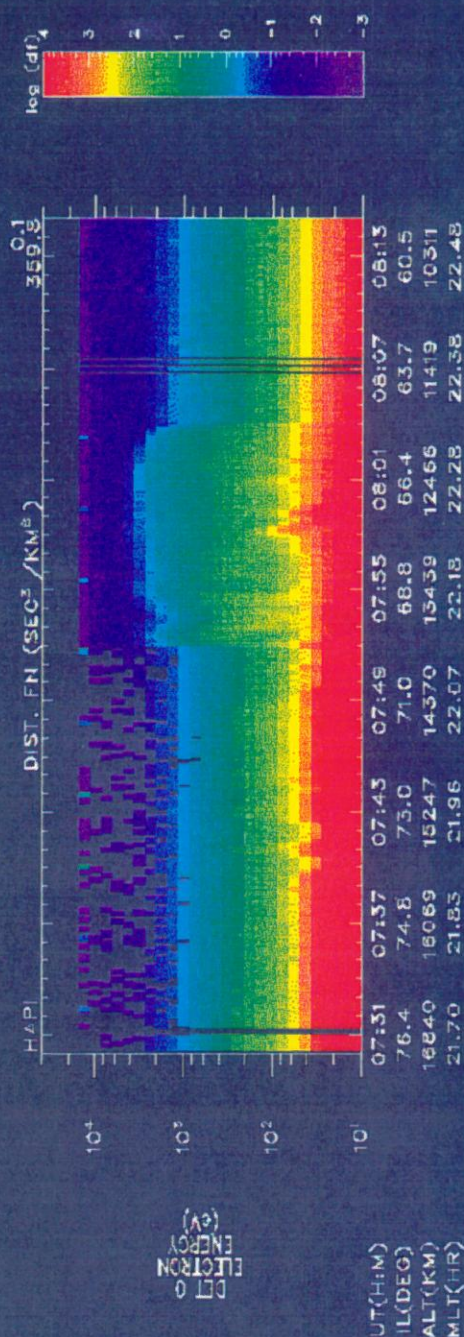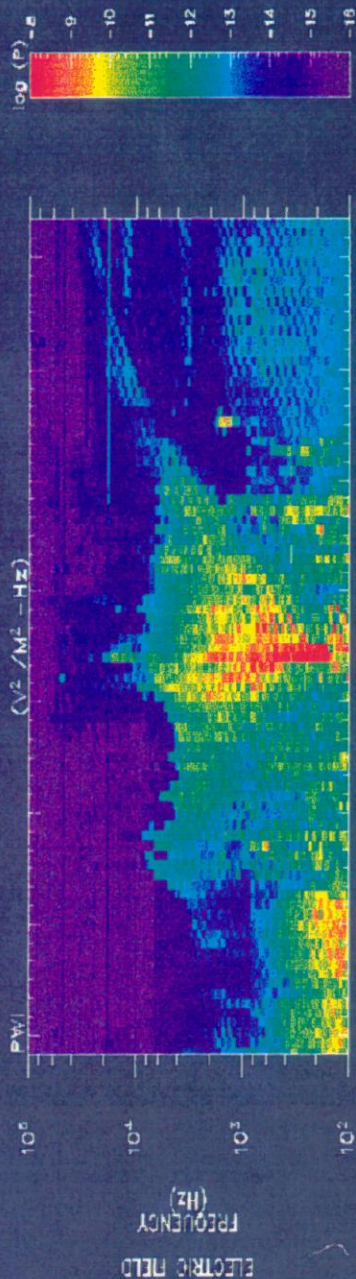
Figure 2.   Spectrogram of auroral hiss event on September 26, 1981.

DYNAMICS EXPLORER
JOINT DATA PRESENTATION
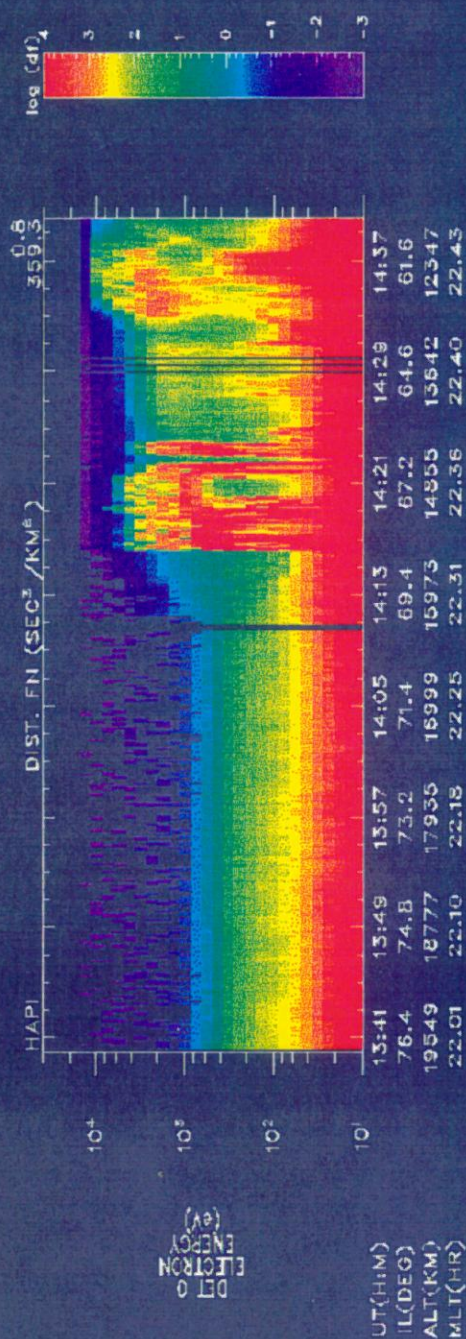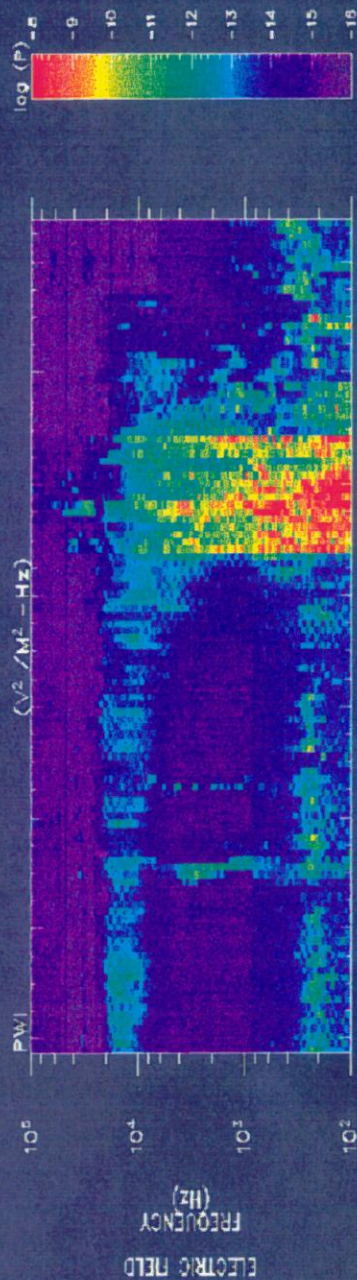
Figure 3.   Spectrogram of auroral hiss event on October 5, 1981.

DYNAMICS EXPLORER
JOINT DATA PRESENTATION
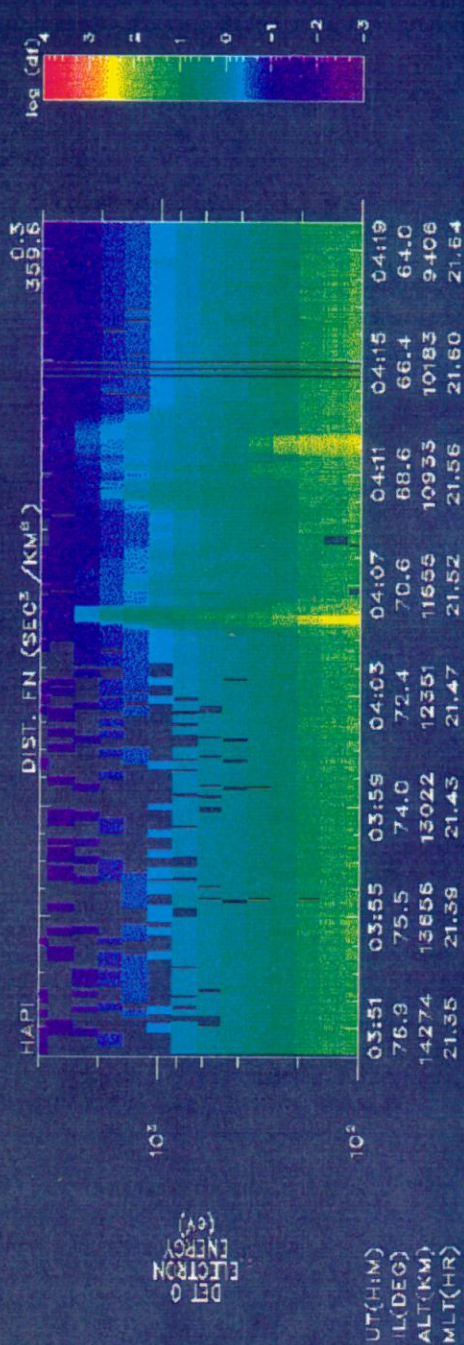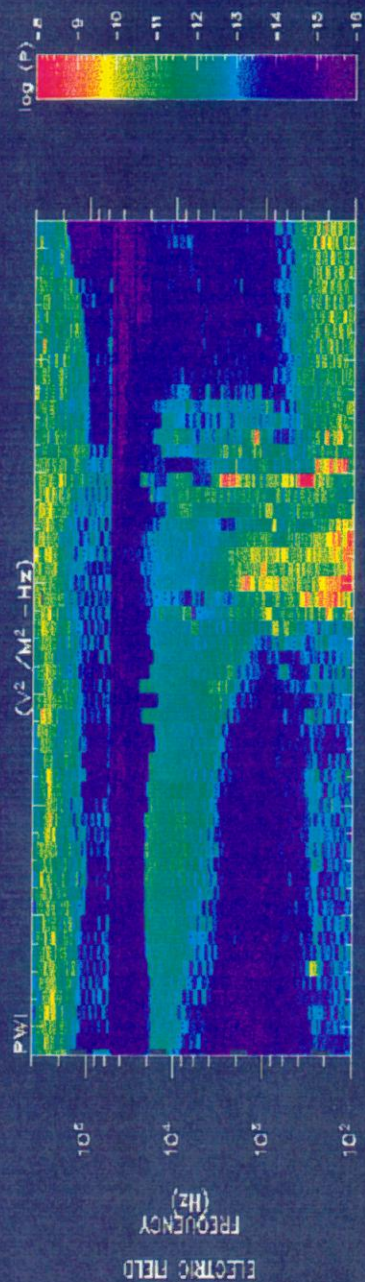
Figure 4.   Spectrogram of a dayside auroral hiss event at 1000 to 1100 UT, September 26, 1981.

DYNAMICS EXPLORER
JOINT DATA PRESENTATION

YR/DAY: 81/269
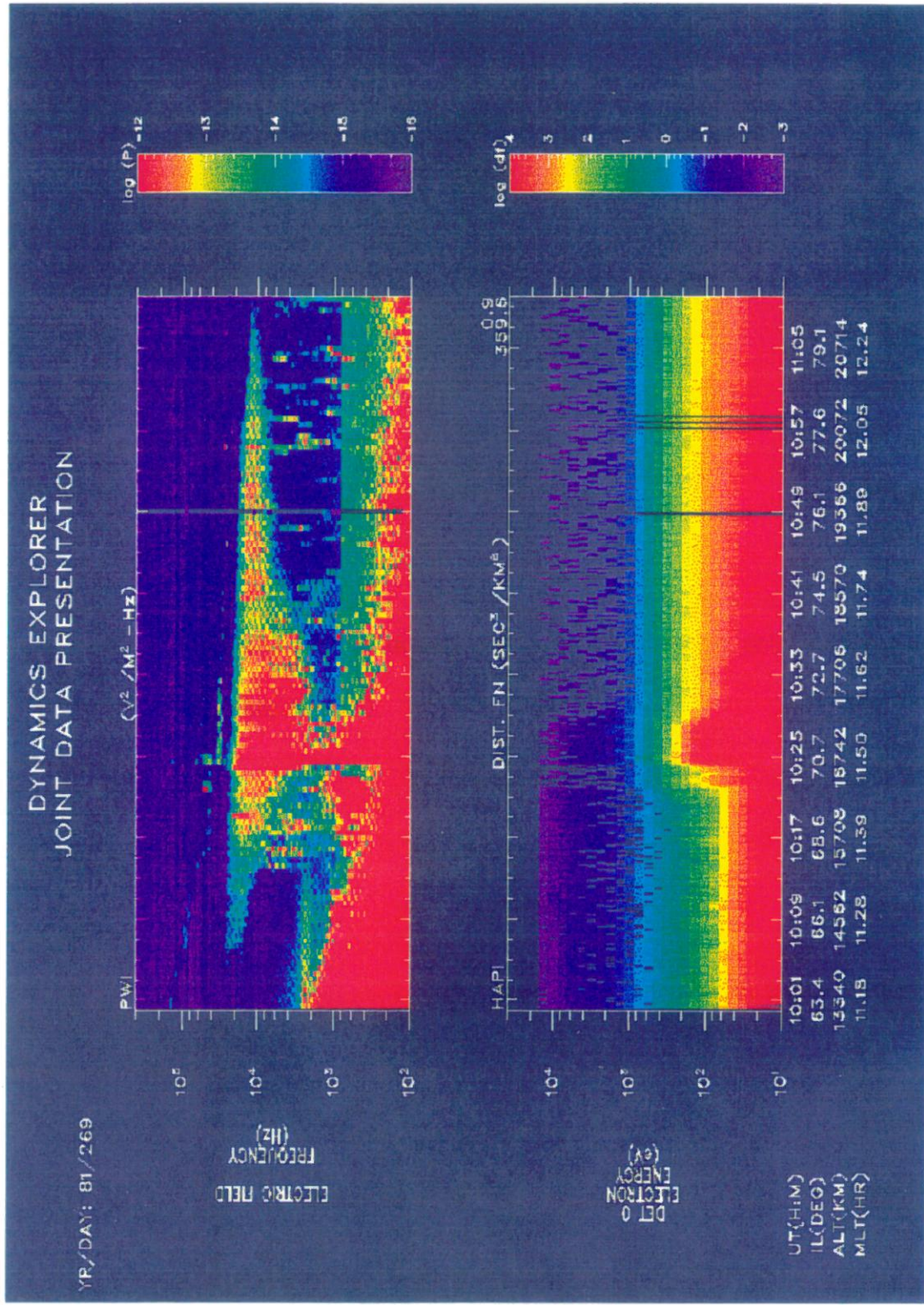
Figure 5.   Contour plot of distribution function over the polar cap for event of October 5, 1981.

DE-1 HAPI ELECTRONS
81278 (5 OCT. 81)
04:02:44.6 TO 04:02:56.3 U.T.

CONTOUR INCREMENT 0.4   CONTOUR FROM -2.4 TO 4.0
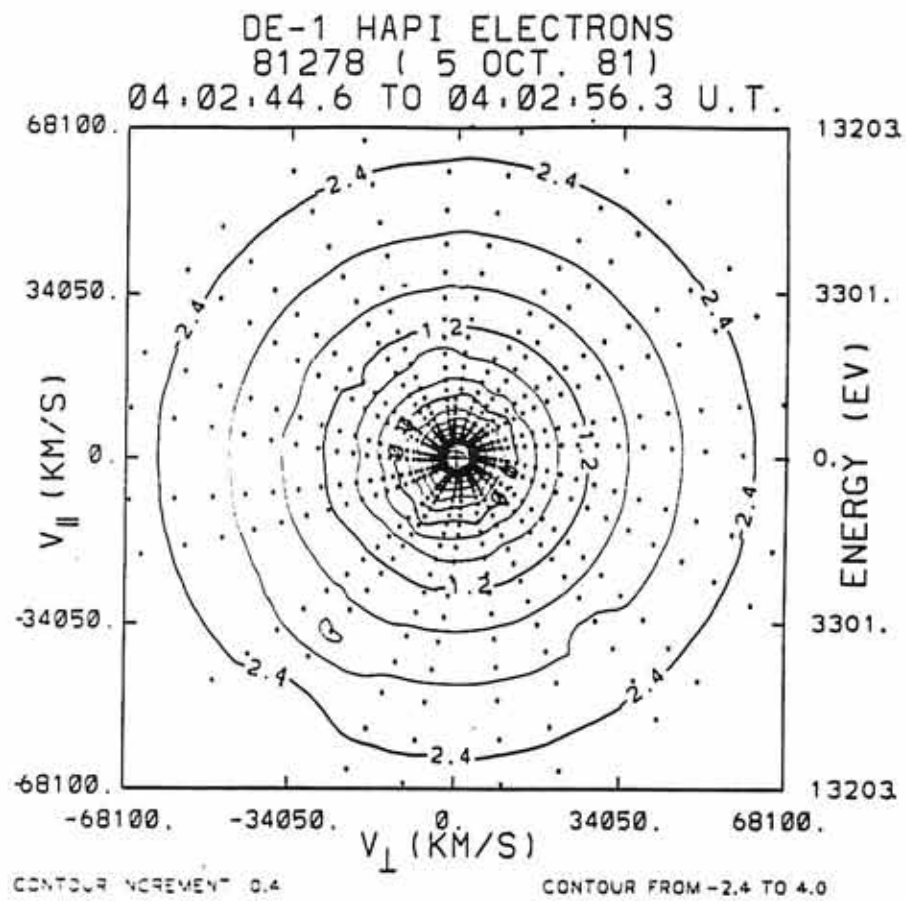
Figure 6.   Contour plot of distribution function over the auroral zone for event of

October 5, 1981.

DE-1 HAPI ELECTRONS
81278 (5 OCT. 81)
04.12.12.3 TO 04.12.24.1 U.T.

CONTOUR INCREMENT 0.4   CONTOUR FROM -2.4 TO 4.4
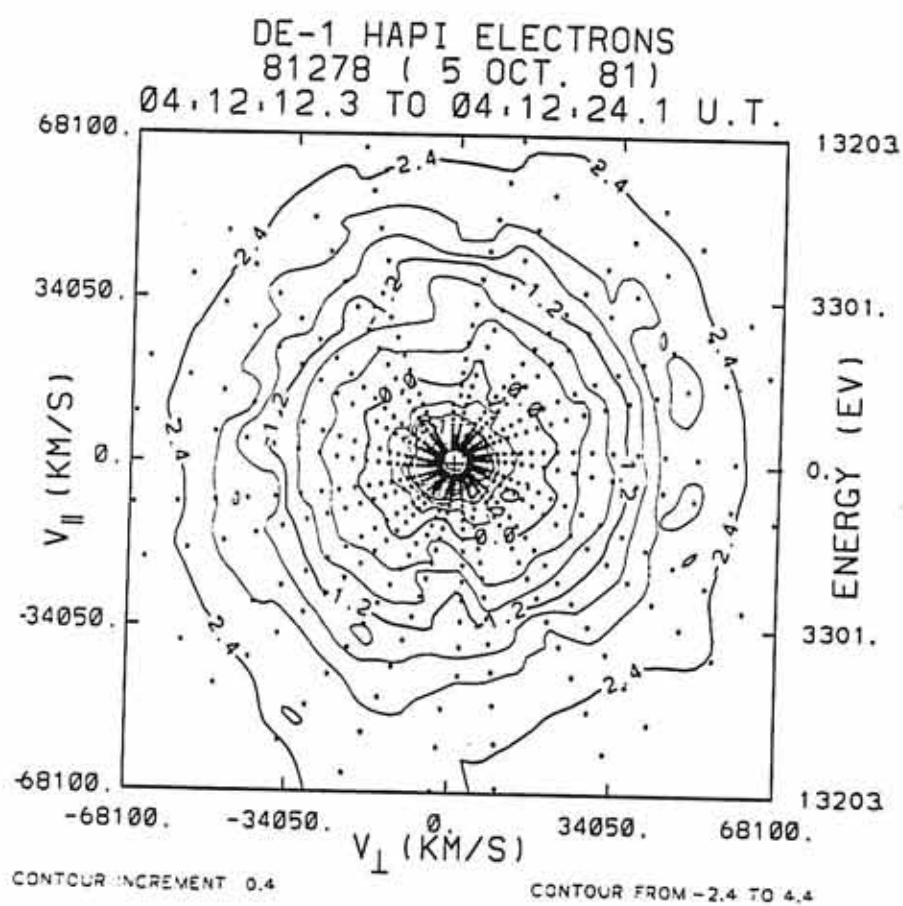
Figure 7.   Contour plot of electron distribution function in the plasma sheet for event of October 5, 1981.

DE-1 HAPI ELECTRONS
81278 (5 OCT. 81)
04.17.06.0 TO 04.17.17.7 U.T.
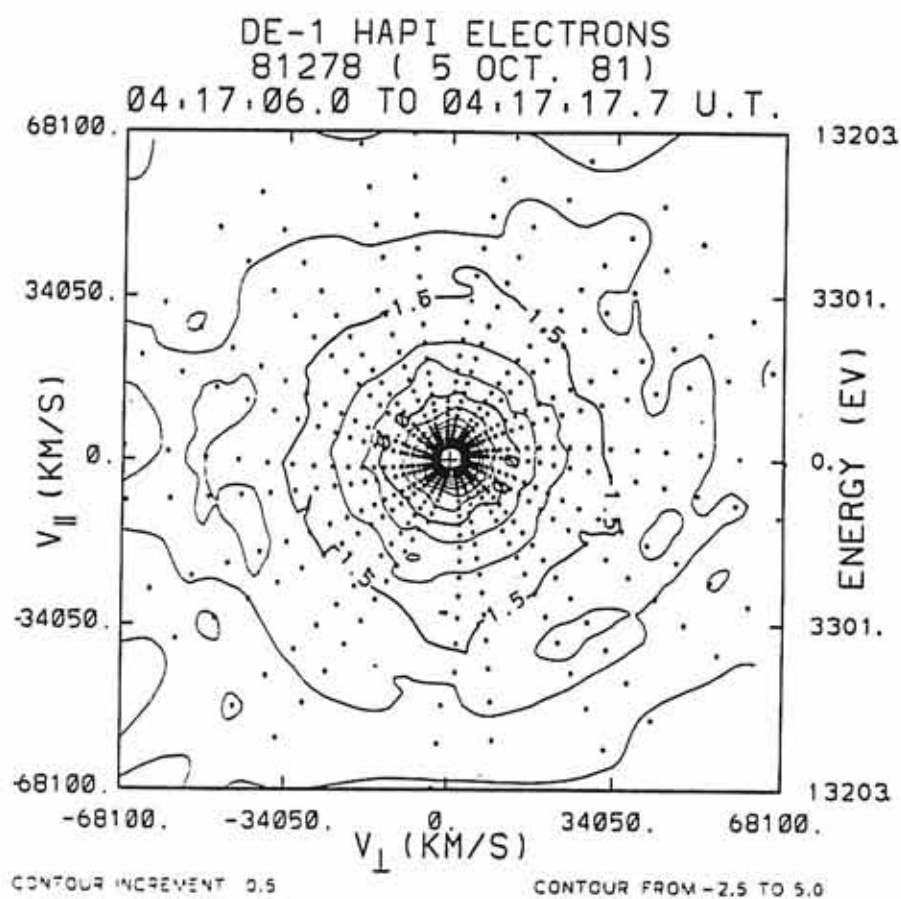
Figure 8.   Log-log plot of an angle and time-averaged distribution function. Several samples of the distribution function over the polar cap have been averaged for event of October 5, 1981.

PITCH-ANGLE AVERAGED DISTRIBUTION-FUNCTION-POLEWARD

B-G92-455

FIT LINE

LOG$_{10}$ PARTICLE ENERGY (eV)

LOG$_{10}$ ELECTRON DISTRIBUTION FUNCTION

(s$_i^3$/km^6)
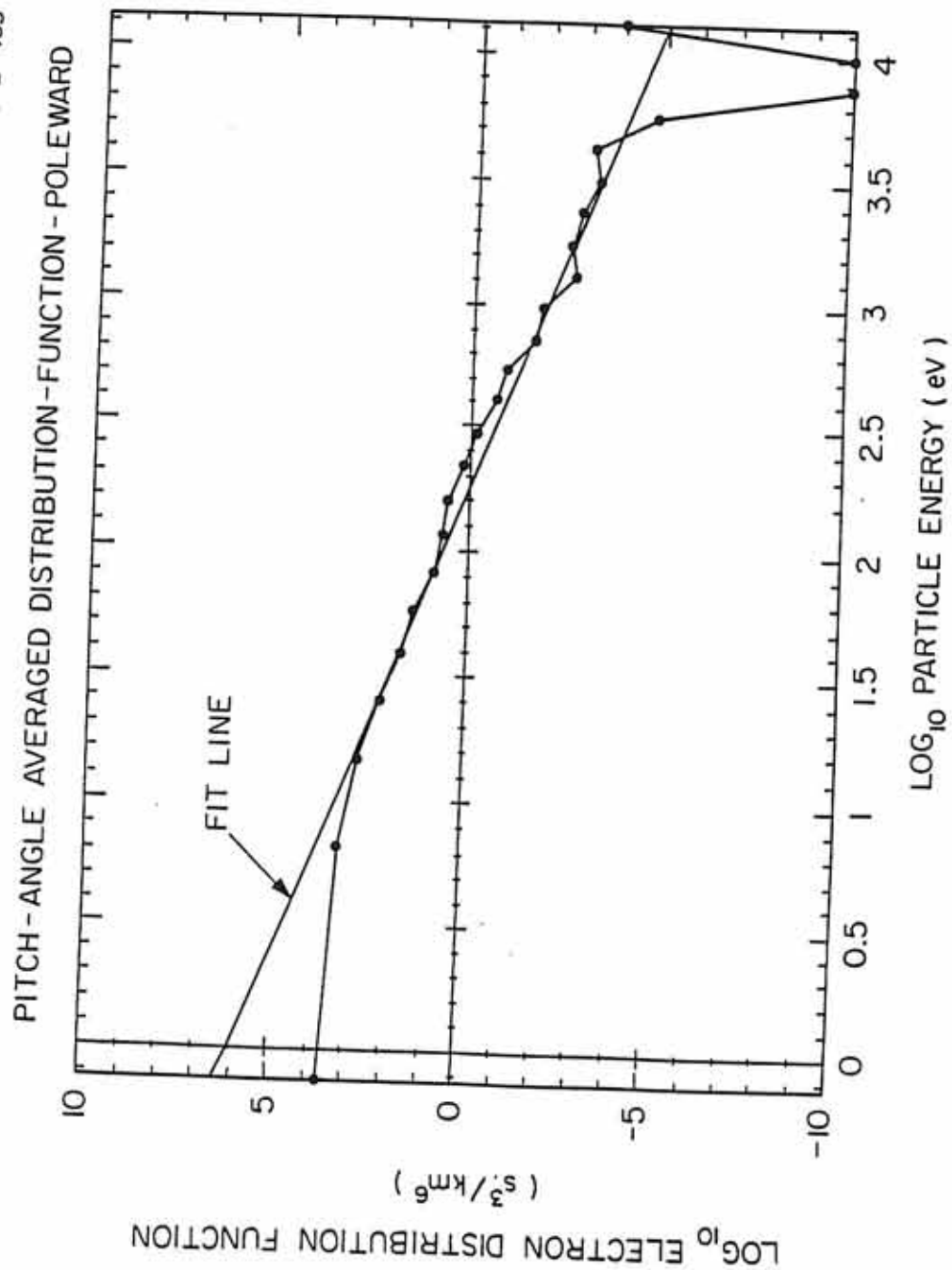
Figure 9.   Log-log plot of angle and time-averaged distribution function from the plasma sheet for event of October 5, 1981.

PITCH-ANGLE AVERAGED DISTRIBUTION FUNCTION – EQUATORWARD

B-G92-456

FIT LINE

LOG$_{10}$ PARTICLE ENERGY (ev)

LOG$_{10}$ ELECTRON DISTRIBUTION FUNCTION (s^3/km^6)
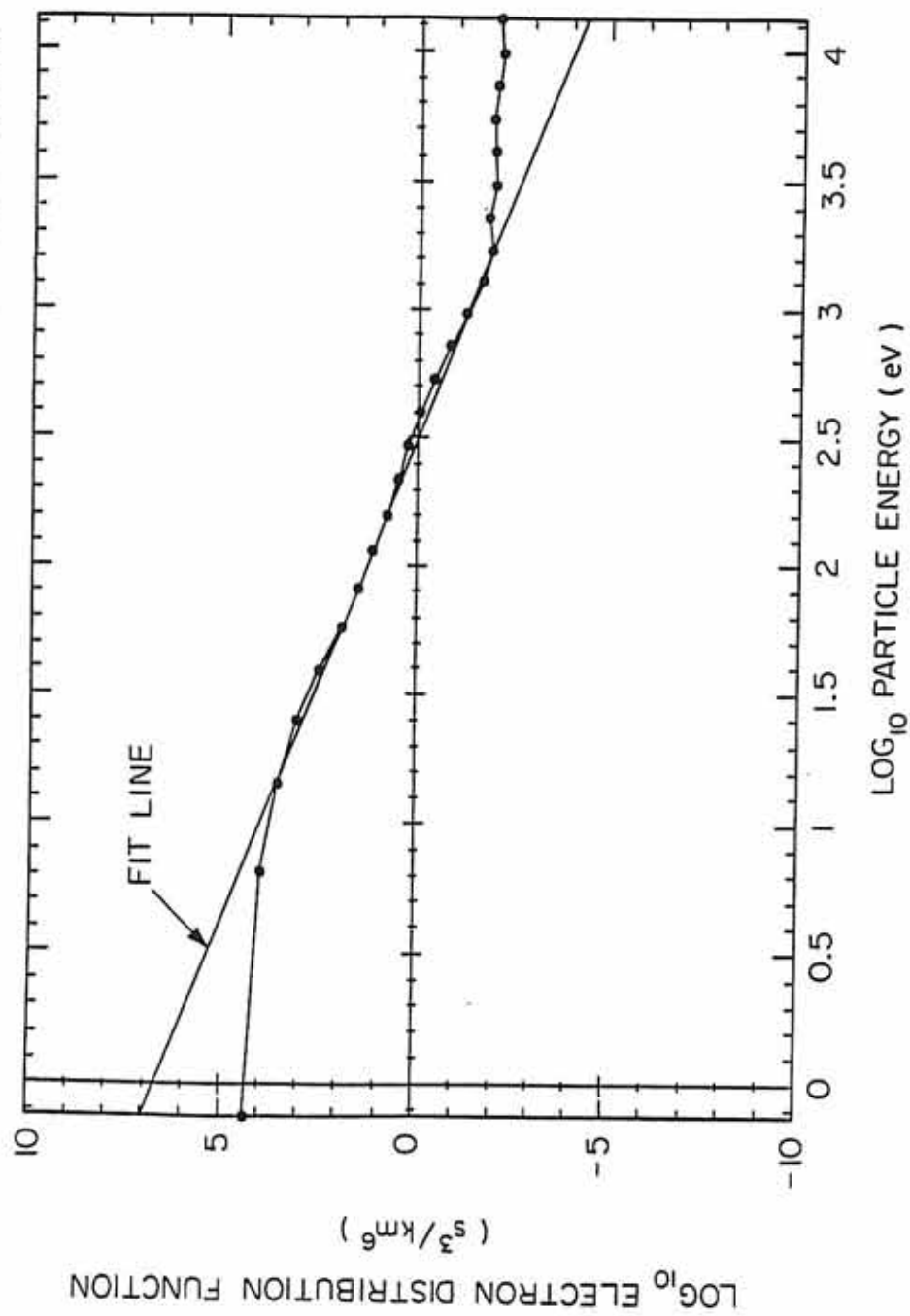
Figure 10. $\partial \mathcal{F} / \partial v_\parallel$ for a sample calculation of γ. The fit line in Figure 8, given by Equation (30b), is the model of the distribution function used.

$\partial F / \partial v_\parallel$ FOR SEVERAL BEAM ENERGIES
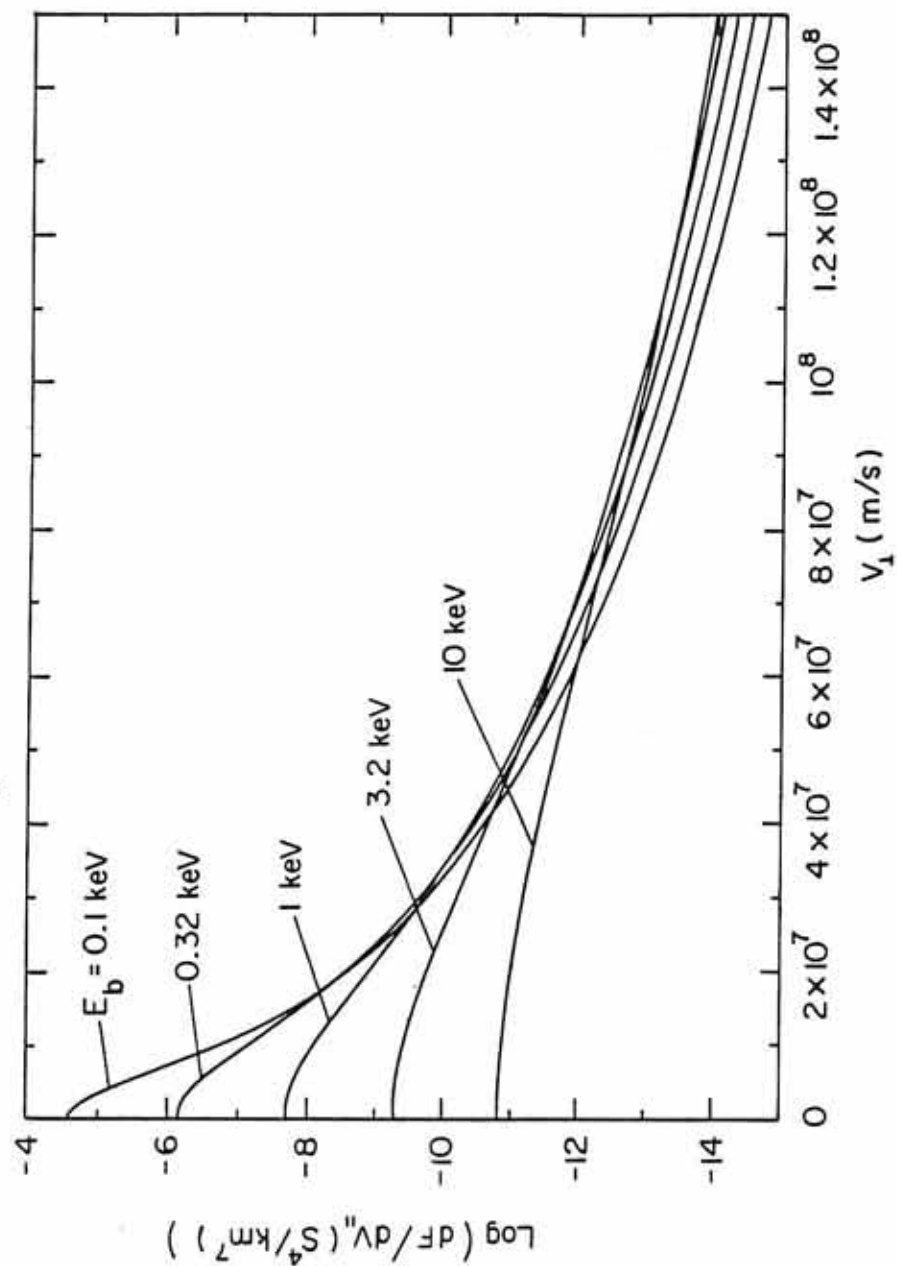
B-G92-457

Figure 11.   The squared Bessel function for sample computations of γ. It is very close to 1 at all relevant values of $v_\perp$.

SQUARE BESSEL WEIGHTING FUNCTION FOR SEVERAL E_b
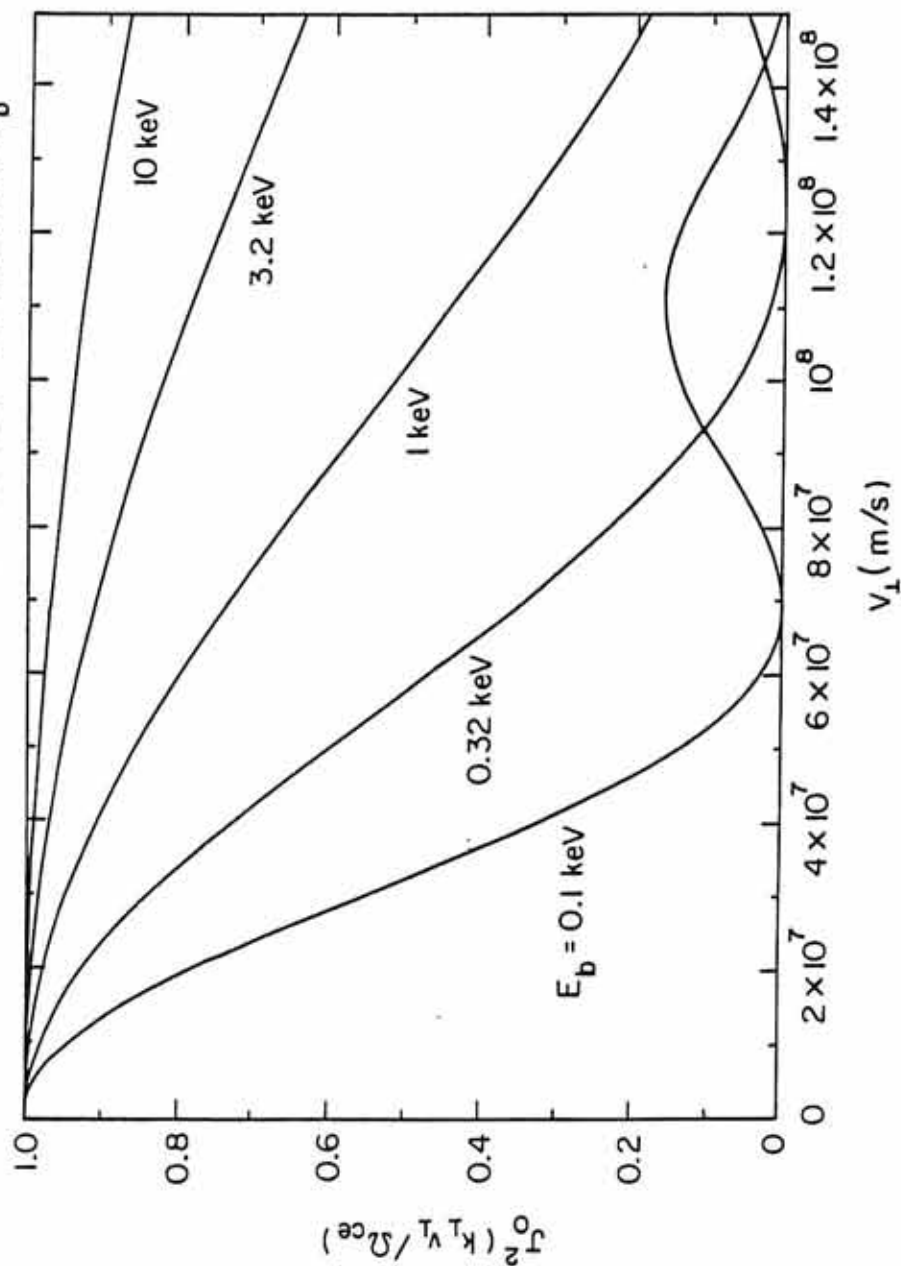
B-G92-458

Figure 12.   Same as Figure 10 except that the model distribution function now has

a loss cone of 10°. The effect of the loss cone is evident only very

close to $v_\perp = 0$.

$\partial F / \partial v_{\parallel}$ FOR SEVERAL E_b WITH 10° LOSS CONE

B-G92-459

$E_b = 0.1$ keV

0.32 keV

1 keV

3.2 keV

10 keV

$V_{\perp}$ (m/s)

Log (dF/dv$_{\parallel}$)
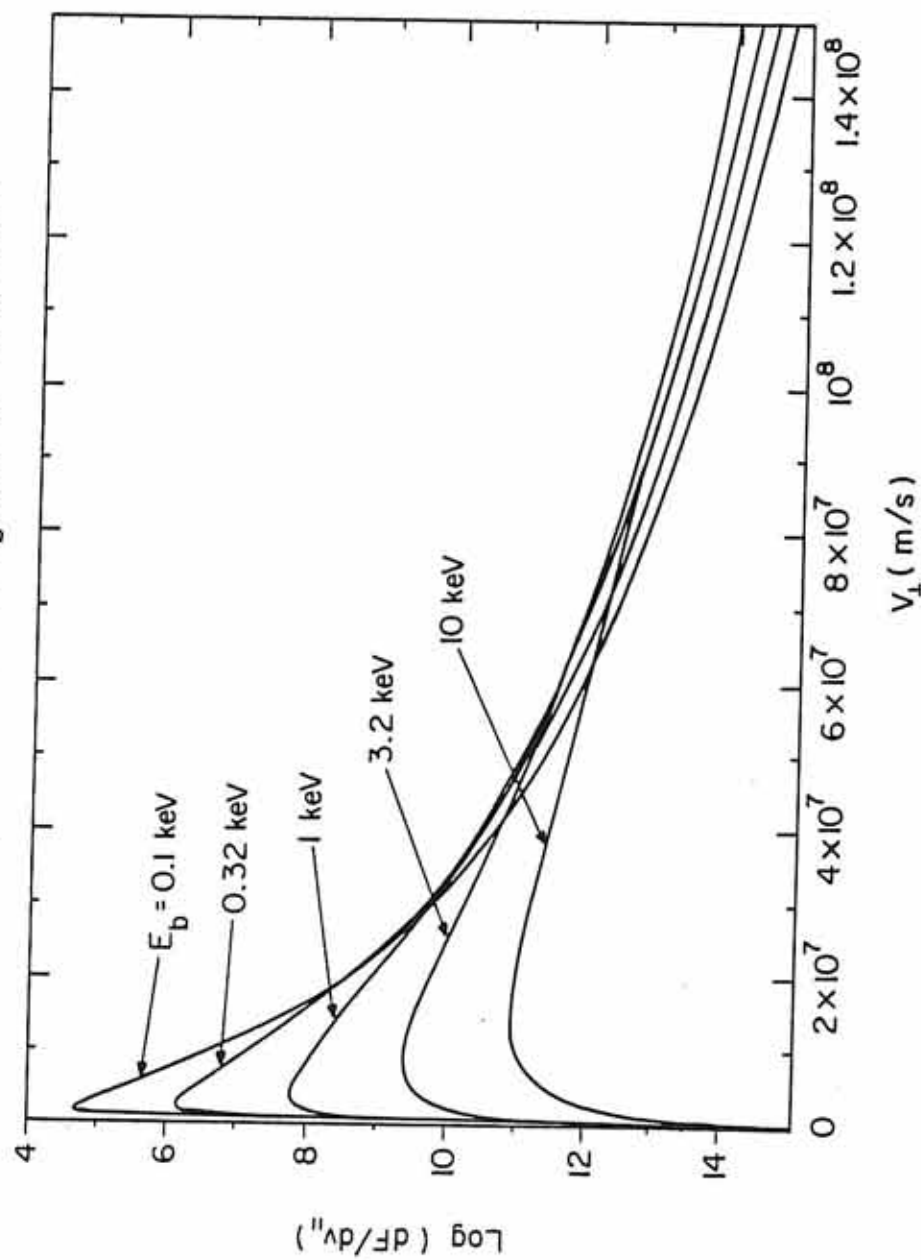
Figure 13.   Schematic diagram illustrating the ray tracing procedure. (a) Progress

of the ray in space. (b) Progress of the index of refraction components.

D-C92-46l

(a)

(b)
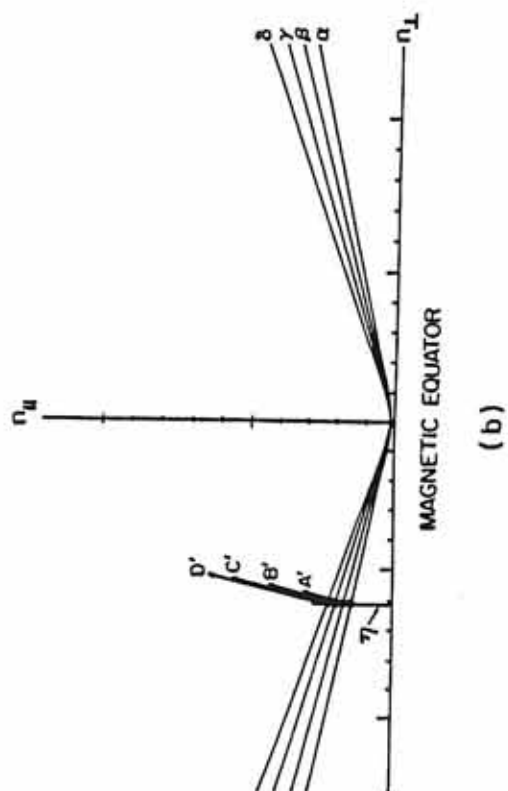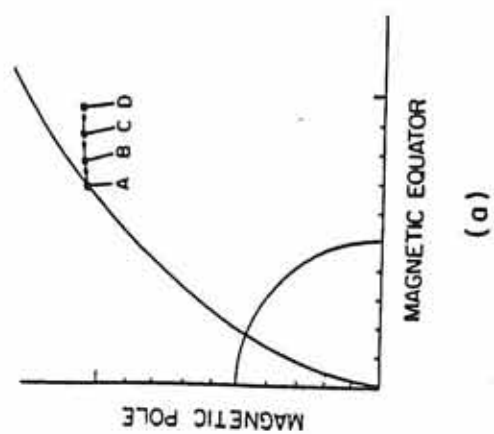
Figure 14.   Error in index of refraction due to using $n_\perp = 0$ as baseline for Poeverlein's construction rather than the line of constant $|B|$. Error is seen to be less than 5%.

C-G92-437

PROGRESS OF INDEX OF REFRACTION - EQUATORWARD
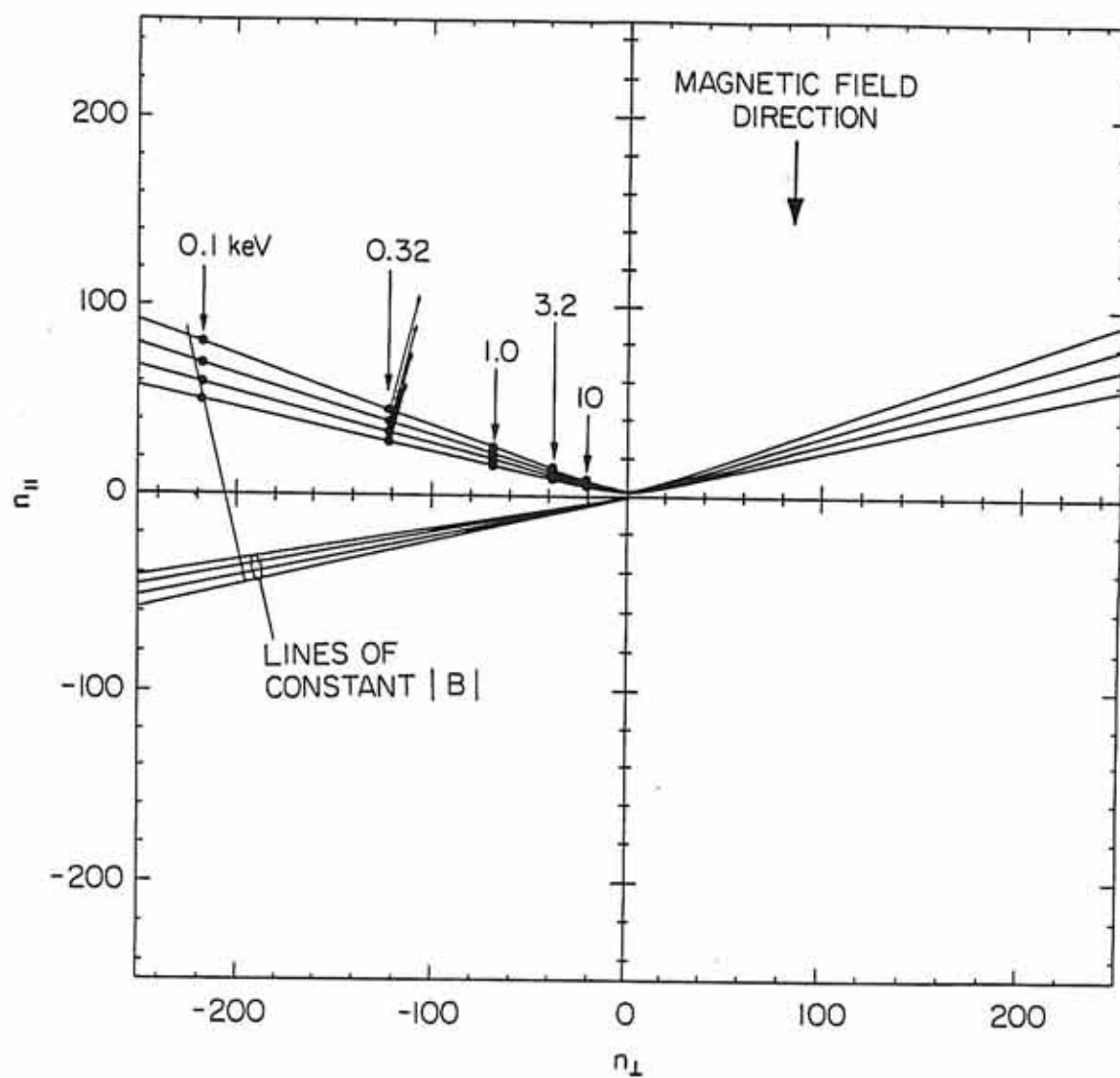
Figure 15.   Effect of variation of beam energy on the ray paths. Notice the effect

is nil since in all cases, the index of refraction is well out on the

resonance cone.

A-G92-440

RAY PATHS - E_b = 0.1, 0.32, 1, 3.2, 10 keV
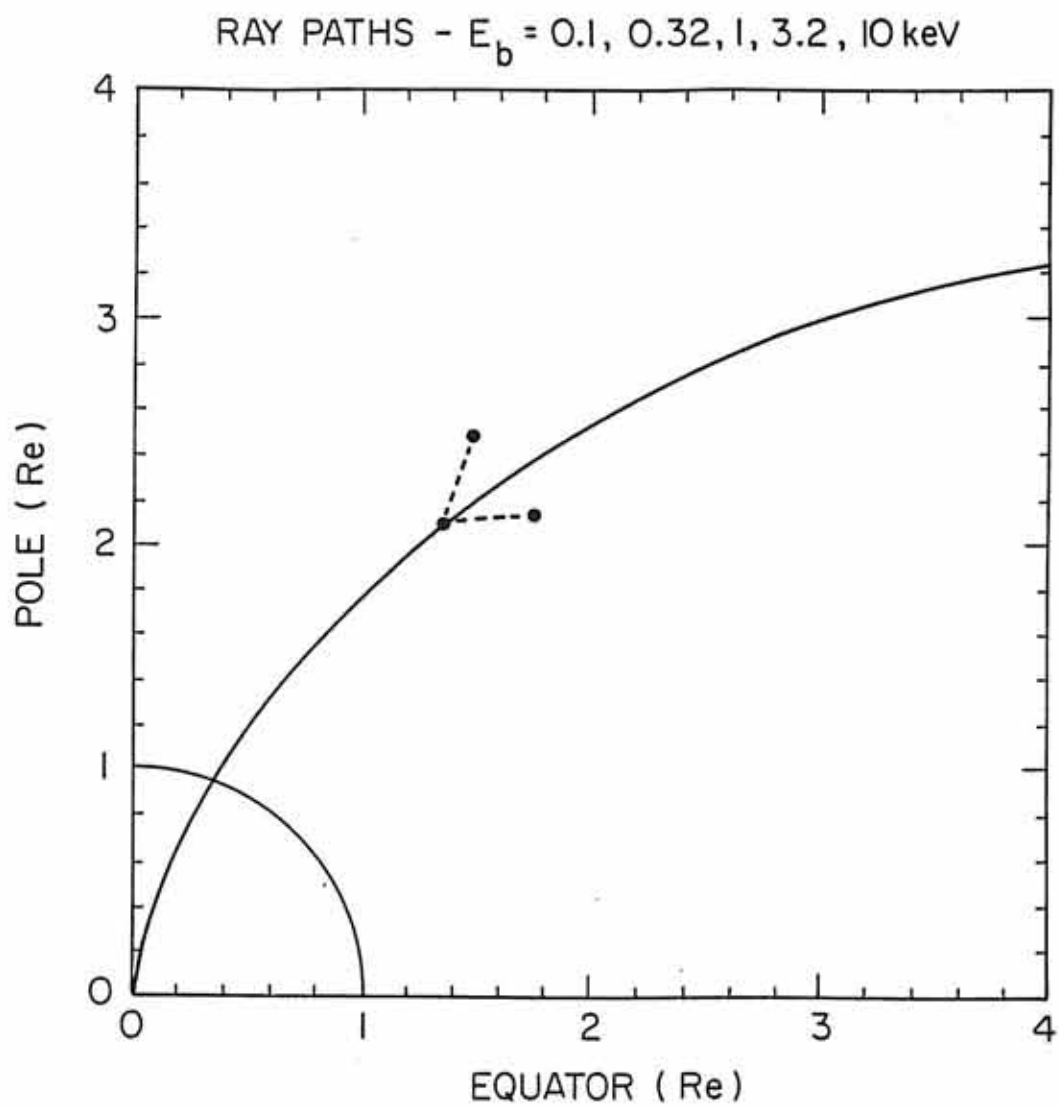
Figure 16.   Growth rates γ for poleward path at 5 values of the beam energy.

GROWTH RATE VARIATION WITH BEAM ENERGY - POLEWARD
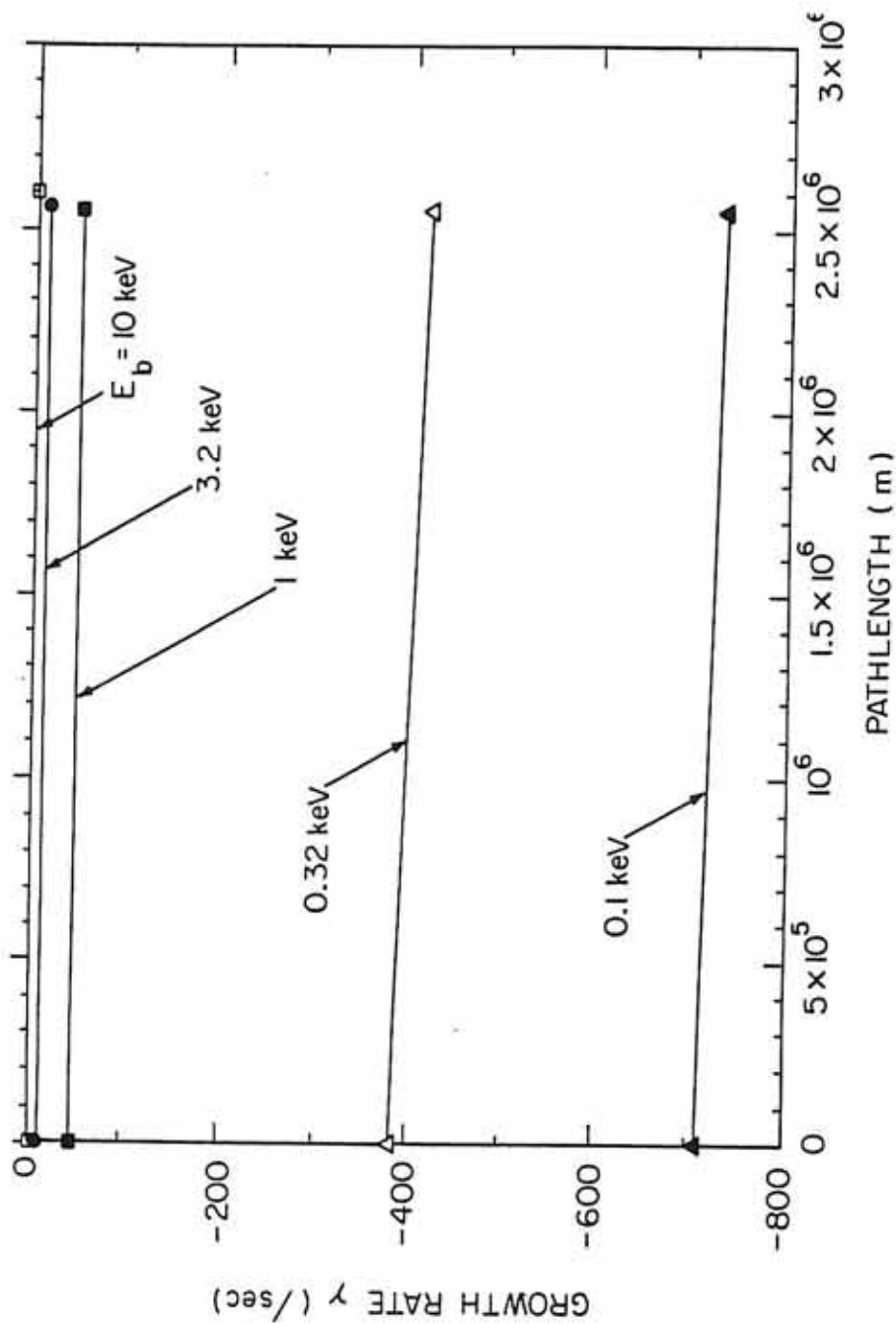
Figure 17.   Integrated growth rates Γ for the poleward path for which γ is shown in
Figure 16.

INTEGRATED GROWTH RATE VARIATION WITH BEAM ENERGY-POLEWARD

B-G92-439
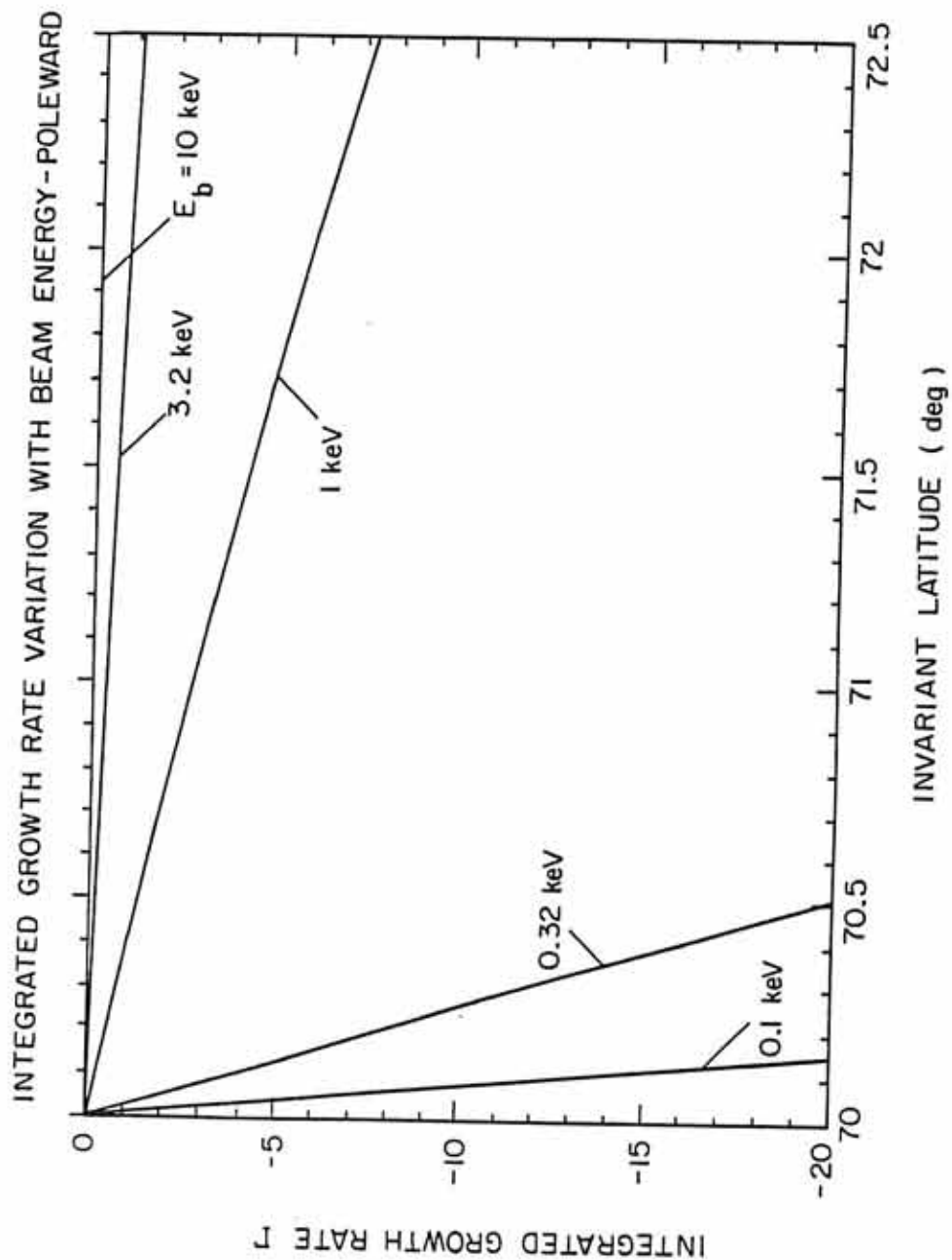
Figure 18.   Growth rates calculated for equatorward path at 5 values of the beam

energy.

GROWTH RATE VARIATION WITH BEAM ENERGY-EQUATORWARD

B-G92-441
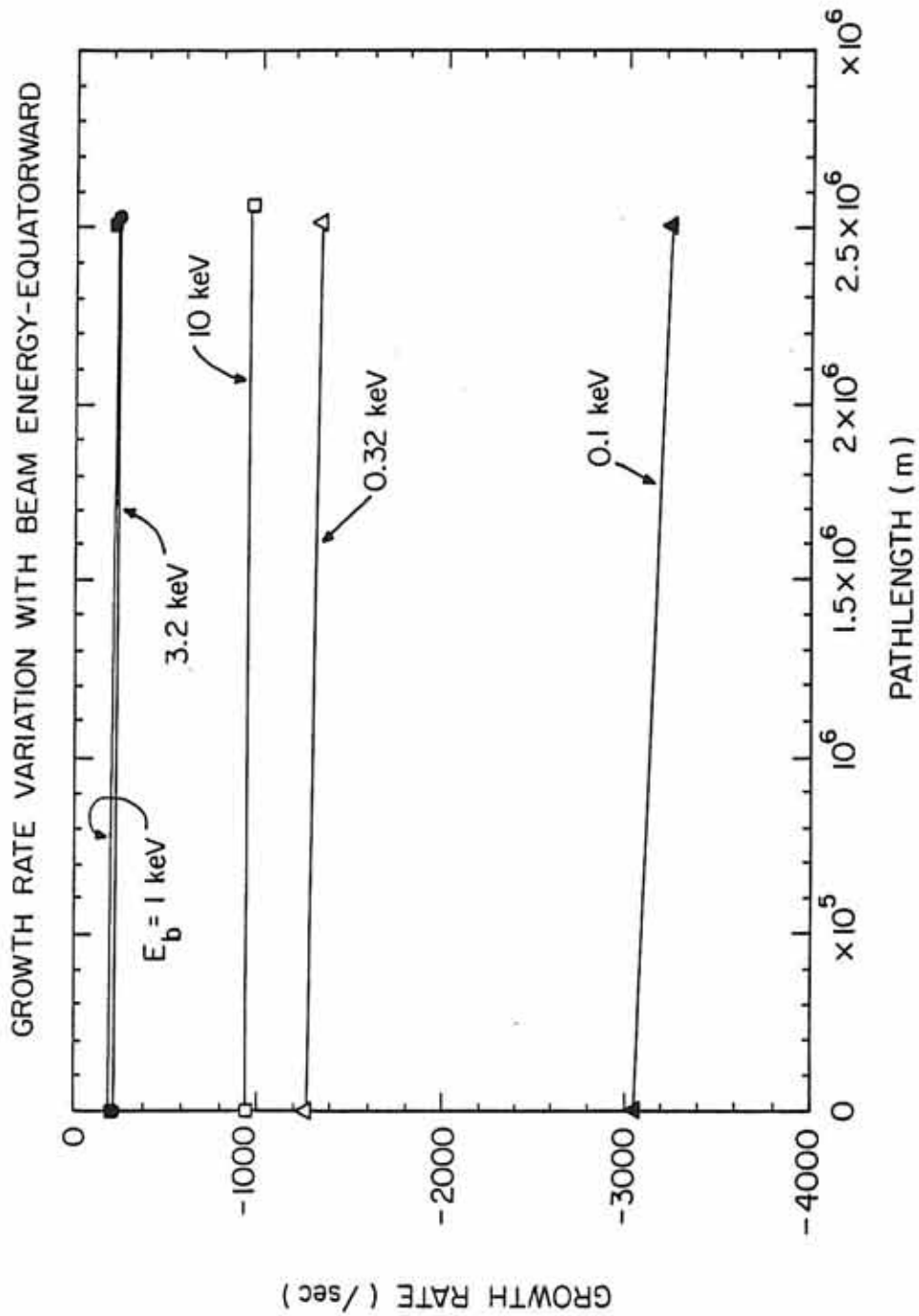
Figure 19.   Integrated growth rates for equatorward path at various energies.

B-G92-442

INTEGRATED GROWTH RATE VARIATION
WITH BEAM ENERGY - EQUATORWARD
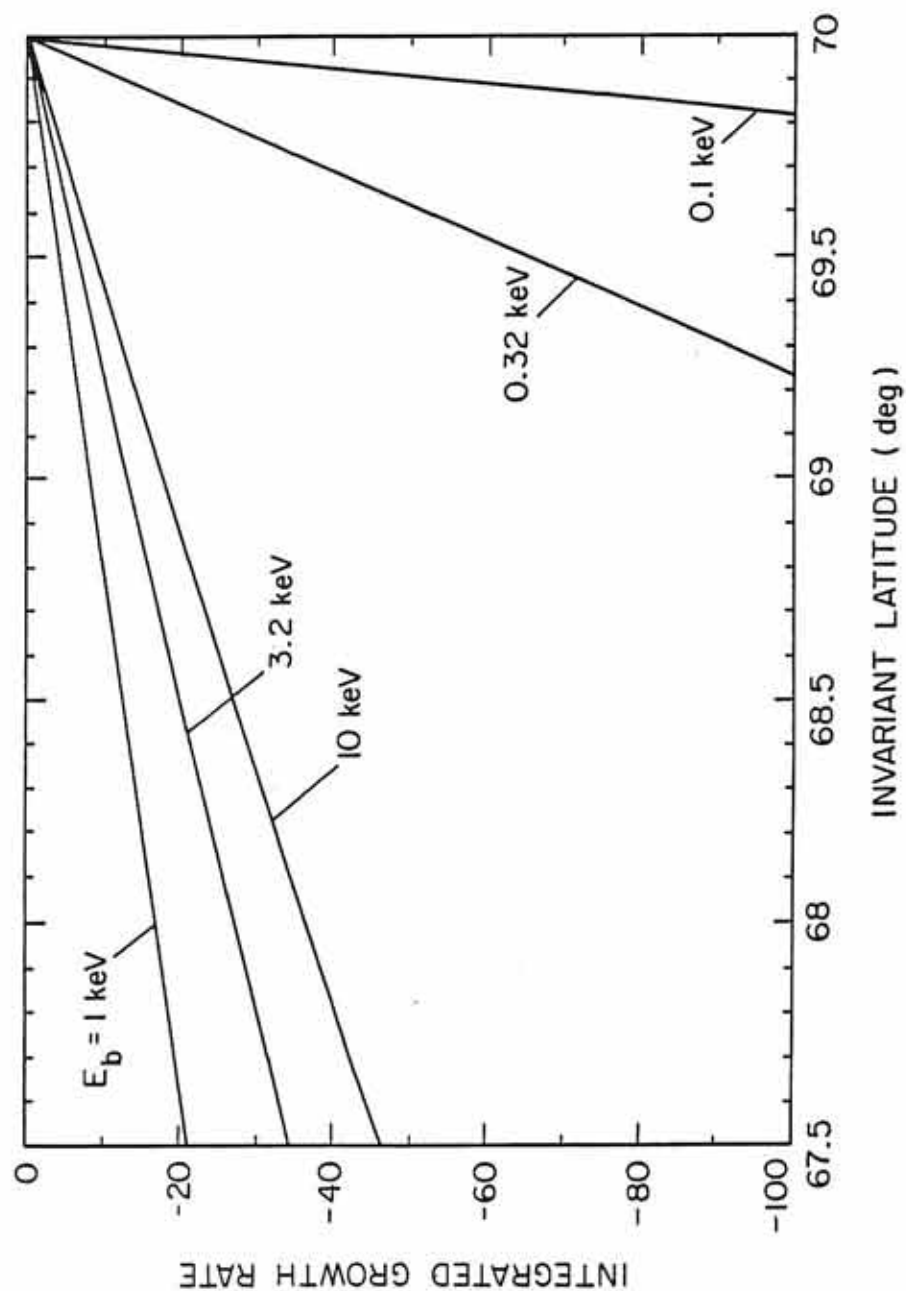
Figure 20.   Ray path variation with frequency.

PATH VARIATION WITH FREQUENCY
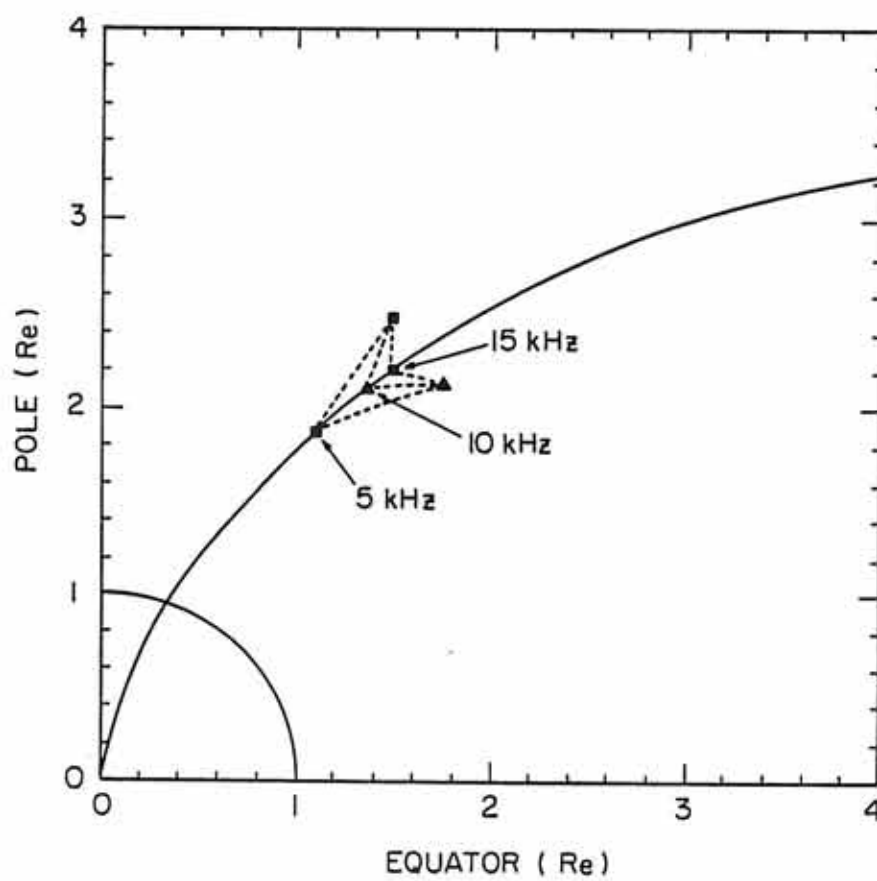
Figure 21.   Growth rate variation with frequency.
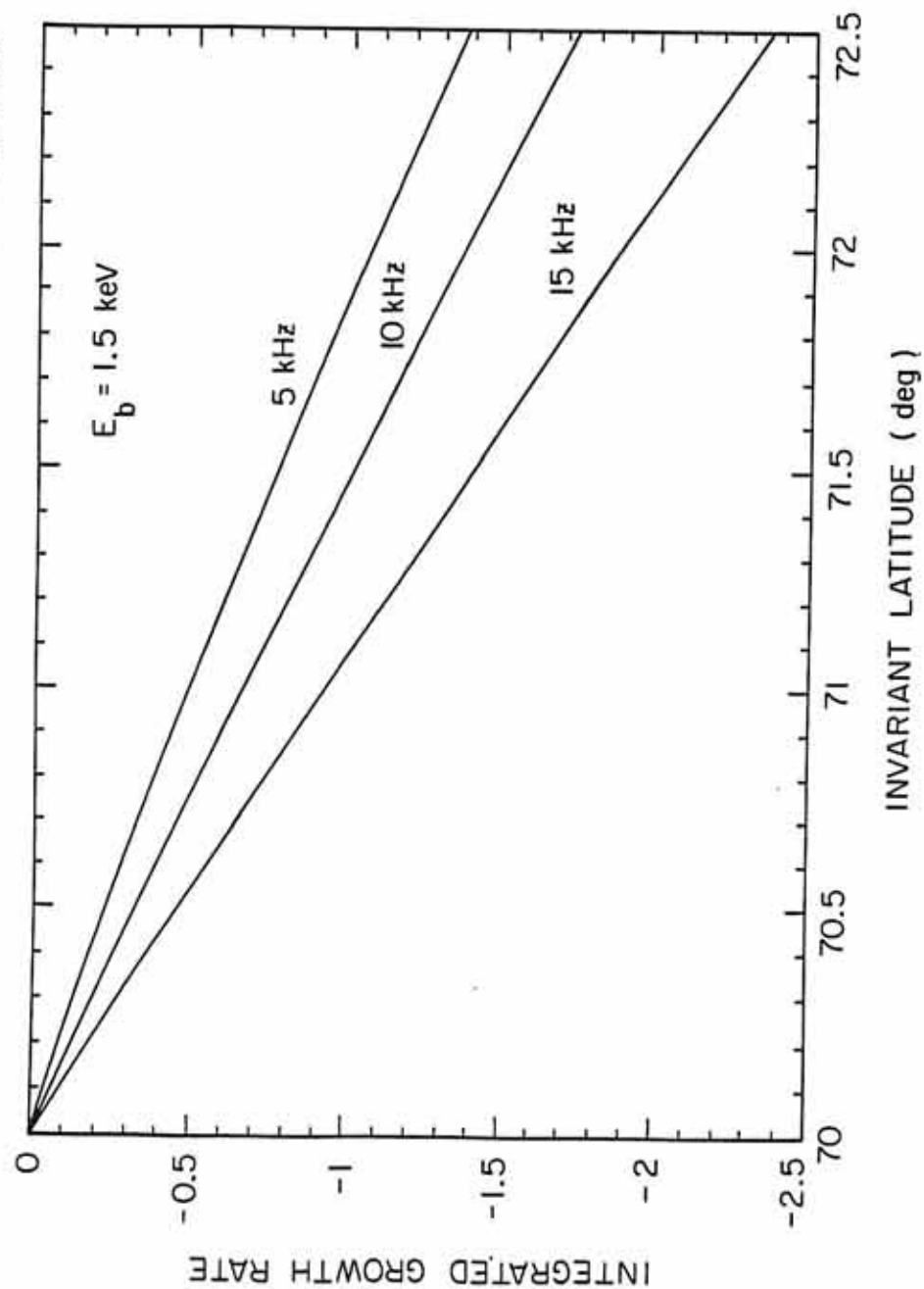
GROWTH RATE VARIATION WITH FREQUENCY - POLEWARD

B-G92-469

$E_b = 1.5$ keV

$f = 5$ kHz

10 kHz

15 kHz

GROWTH RATE (/s)

PATHLENGTH (m)
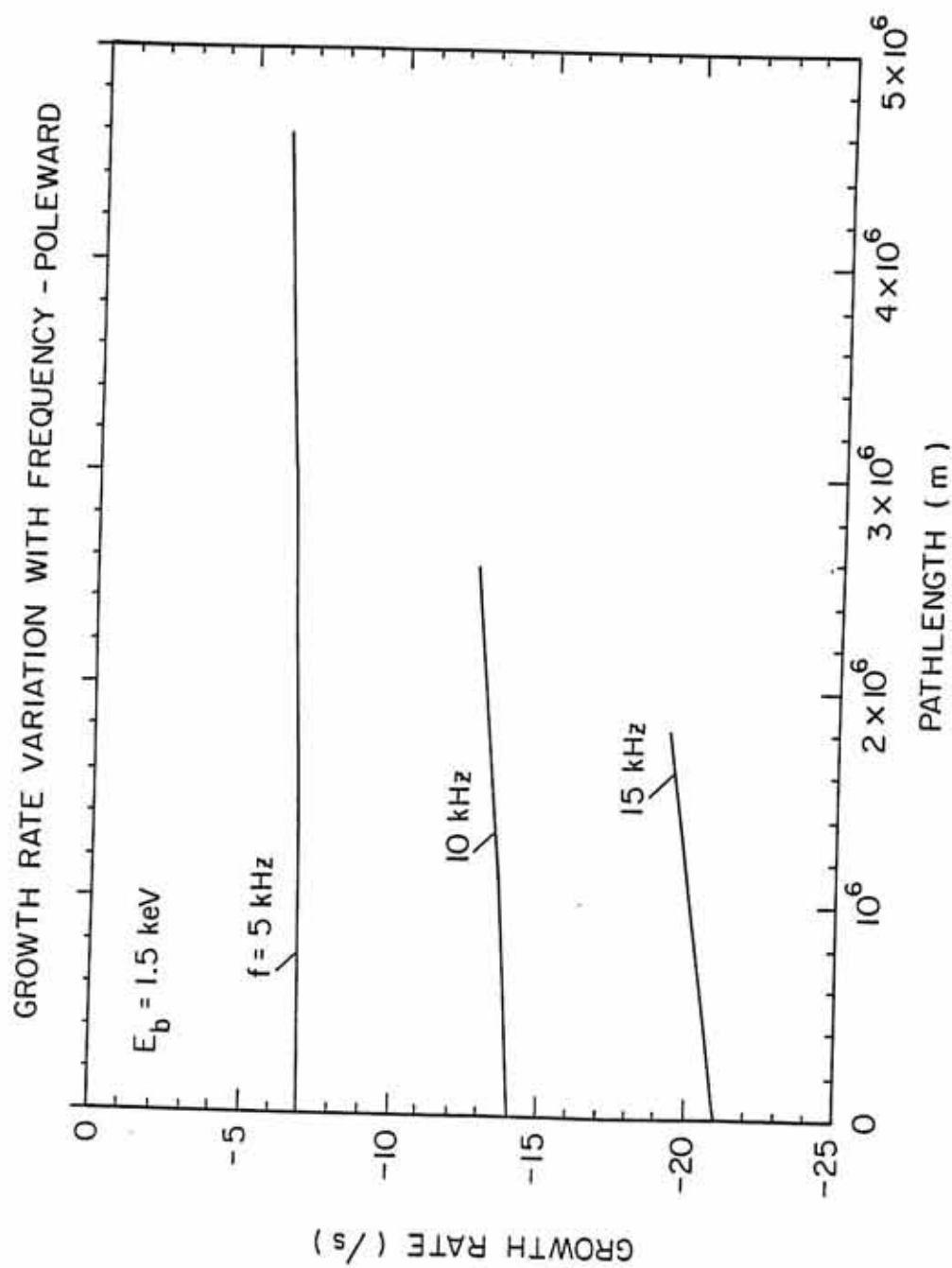
Figure 22.   Integrated growth rate variation with frequency.

INTEGRATED GROWTH RATE VARIATION WITH FREQUENCY - POLEWARD

B-G92-470

$E_b = 1.5$ keV

5 kHz

10 kHz

15 kHz

INVARIANT LATITUDE (deg)

INTEGRATED GROWTH RATE

Figure 23.   Possible mechanism for converting whistler mode radiation generated by

a 100 eV beam into radiation with small enough wavenumber to escape

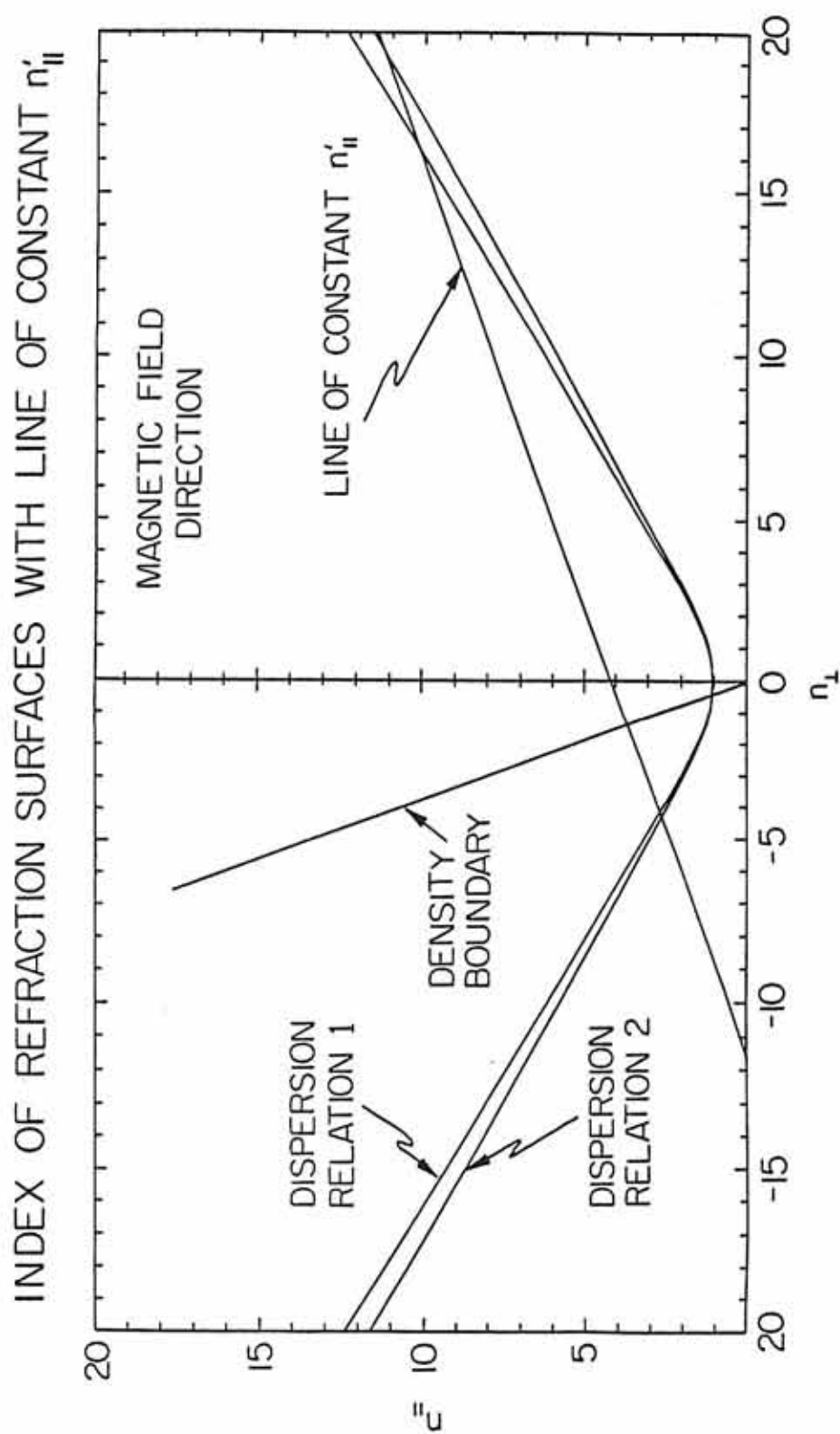damping. Density fluctuation is perpendicular to line of constant $n_{\parallel}'$,

20° from the magnetic field line.

INDEX OF REFRACTION SURFACES WITH LINE OF CONSTANT $n'_\parallel$

C-G92-369

108

Figure 24.   A multiple reflection mechanism involving a density cavity oblique to the magnetic field. In this situation, t_1 and subsequent odd transmitted rays will be of short wavelength and will therefore be damped. On the other hand, t_2 and subsequent even numbered transmitted rays will be of long wavelength and will propagate without damping.
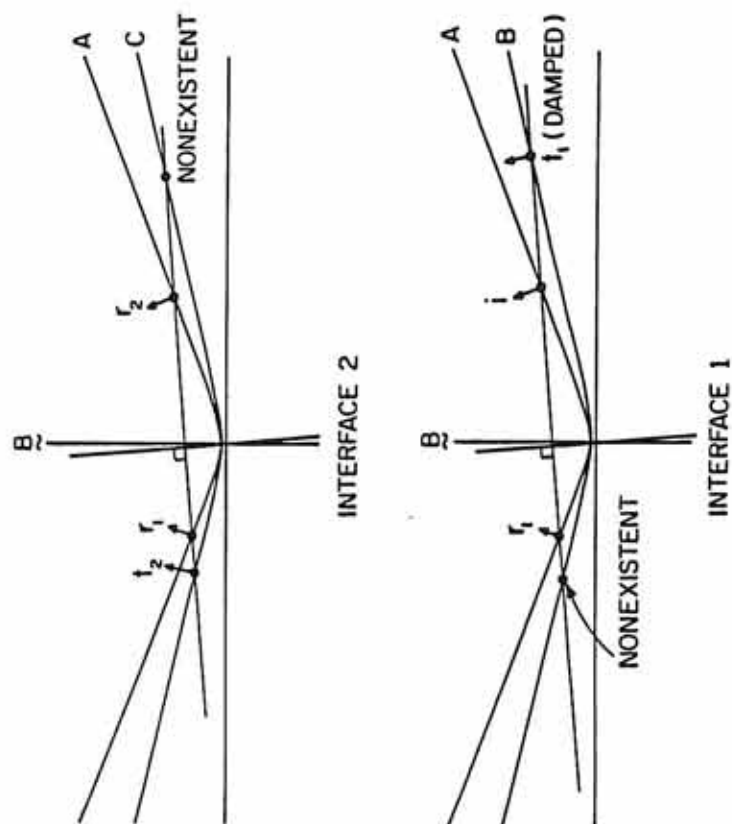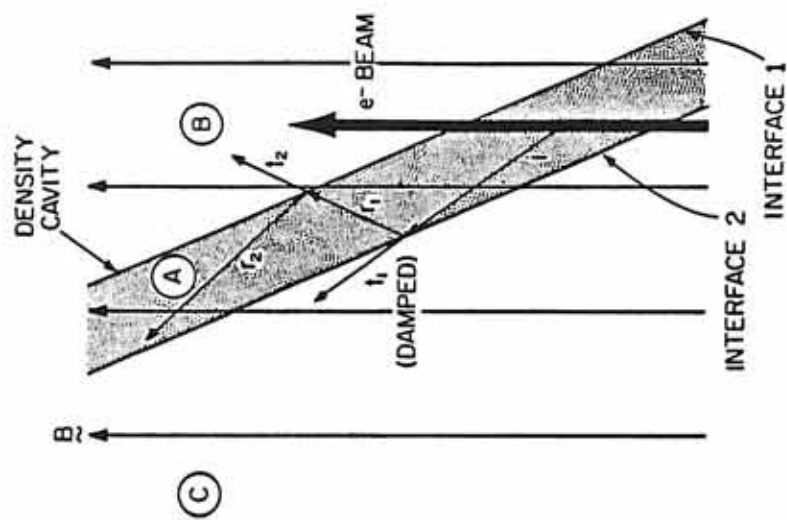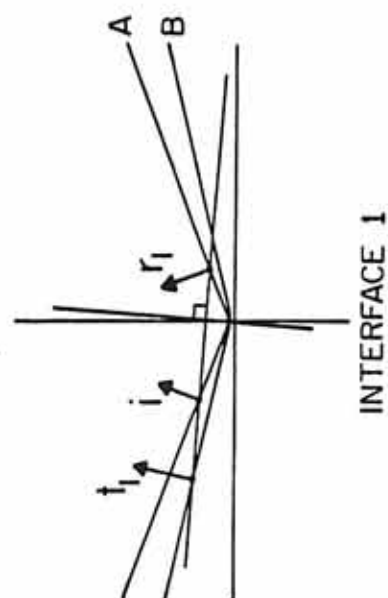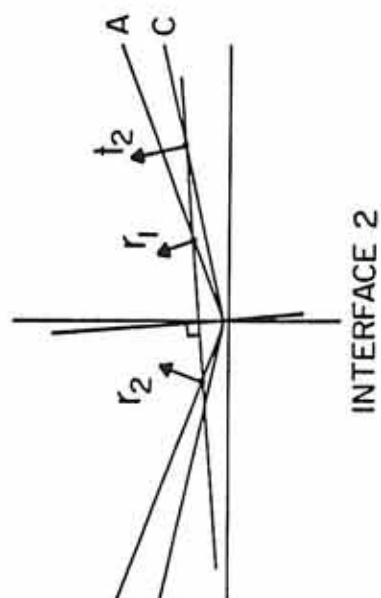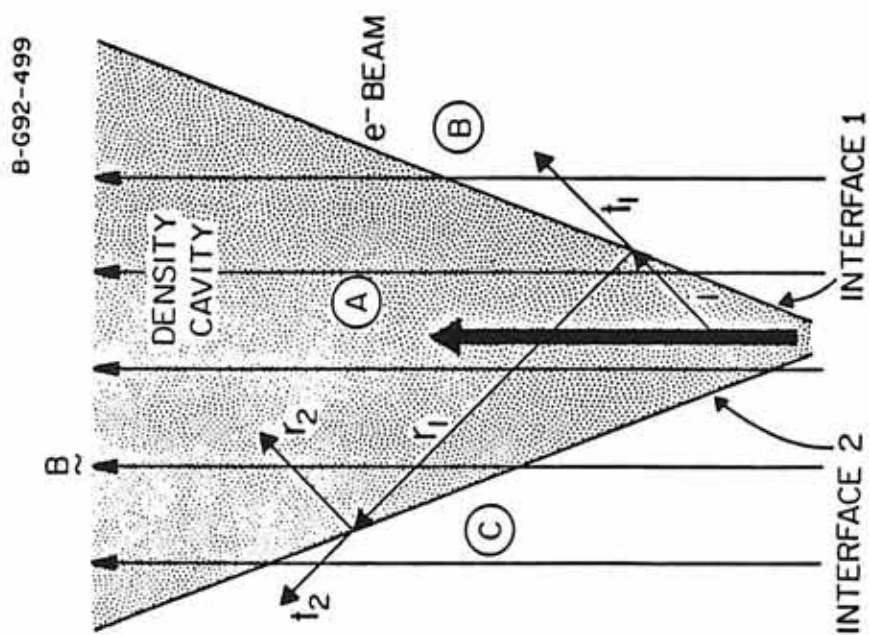
Figure 25.   A multiple reflection mechanism involving a flared density cavity. In this situation, each reflection causes a lengthening of the wavelength of the reflected ray. Thus a ray undergoing several reflections could have a significantly increased wavelength even if the angle of flaring of the density cavity is quite small.

REFERENCES

Bell, T. F., and H. D. Ngo, Electrostatic lower hybrid waves excited by electromagnetic whistler mode waves scattering from planar magnetic-field aligned plasma density irregularities, J. Geophys. Res., 95, 149, 1990.

Borovsky, J. E., and G. Joyce, The simulation of plasma double layer structures in two dimensions, J. Plasma Phys., 29, 45, 1983.

Budden, K. G., The Propagation of Radio Waves, Cambridge Univ. Press, Cambridge, 1985.

Burch, J. L., J. D. Winningham, V. A. Blevins, N. Eaker, W. C. Gibson, and R. A. Hoffman, High-altitude plasma instrument for Dynamics Explorer-A, Space Sci. Instrum., 5, 455, 1981.

Burton, E. T., and E. M. Boardman, Audio-frequency atmospherics, Proc. Inst. Radio Engrs., 21, 1476, 1933.

Farrell, W. M., D. A. Gurnett, P. M. Banks, R. I. Bush, and W. J. Raitt, An analysis of whistler mode radiation from the Spacelab 2 electron beam, J. Geophys. Res., 93, 153, 1988.

Farrell, W. M., D. A. Gurnett, and C. K. Goertz, Coherent Cerenkov radiation from the Spacelab 2 electron beam, J. Geophys. Res., 94, 443, 1989.

Garrett, H. B., Spacecraft charging: a review, in "Space Systems and Their Interactions with Earth's space Environment" (H. B. Garrett and C. P. Pike, eds.), Progress in Astronautics and Aeronautics, Vol. 71, p. 167, 1980.

Gurnett, D. A., A satellite study of VLF hiss, J. Geophys. Res., 71, 5599, 1966.

Gurnett, D. A., and L. A. Frank, VLF hiss and related plasma observations in the polar magnetosphere, J. Geophys. Res., 77, 172, 1972.

Gurnett, D. A., and L. A. Frank, A region of intense plasma wave turbulence on auroral field lines, J. Geophys. Res., 82, 1031, 1977.

Gurnett, D. A., and U. S. Inan, Plasma wave observations with the Dynamics Explorer 1 spacecraft, Rev. Geophys., 26, (2), 285, 1988.

Gurnett, D. A., W. S. Kurth, J. T. Steinberg, P. M. Banks, R. I. Bush, and W. J. Raitt, Whistler-mode radiation from the Spacelab 2 electron beam, Geophys. Res. Lett., 13, (3), 225, 1986.

Gurnett, D. A., S. D. Shawhan, and R. R. Shaw, Auroral hiss, Z mode radiation, and auroral kilometric radiation in the polar magnetosphere: DE 1 observations, J. Geophys. Res., 88, 329, 1983.

Helliwell, R. A., Whistlers and Related Ionospheric Phenomena, Stanford University Press, Stanford, California, 1965.

Hilgers, A., The auroral radiating plasma cavities, Geophys. Res. Lett., 19, (3), 237, 1992.

James, H. G., VLF saucers, J. Geophys. Res., 81, 501, 1981.

Kennel, C., Low-frequency whistler mode, Phys. Fluids, 9, (11), 2190, 1966.

Landau, L. D., J. Phys. (U.S.S.R.), 10, 25, 1946.

Lin, C. S., J. L. Burch, S. D. Shawhan, and D. A. Gurnett, Correlation of auroral hiss and upward electron beams near the polar cusp, J. Geophys. Res., 89, 925, 1984.

Morozumi, H. M., A study of the aurora australis in connection with an association between VLFE hiss and auroral arcs and bands observed at south geographical pole 1960, M. S. Thesis, Univ. of Iowa, Iowa City, Iowa.

Mosier, S. R., and D. A. Gurnett, VLF measurements of the Poynting flux along the geomagnetic field with the Injun 5 satellite, J. Geophys. Res., 74, 5675, 1969.

Smith, R. L., VLF observations of auroral beams as sources of a class of emission, Nature, 224 (5217), 351, 1969.

Stix, T. H., The Theory of Plasma Waves, McGraw-Hill, New York, 1962.

Taylor, W.W.L., Generation and propagation of electromagnetic waves in the magnetosphere, Ph.D. Thesis, University of Iowa, Iowa City, Iowa, 1973.